106學年度

學生專題研究論文集

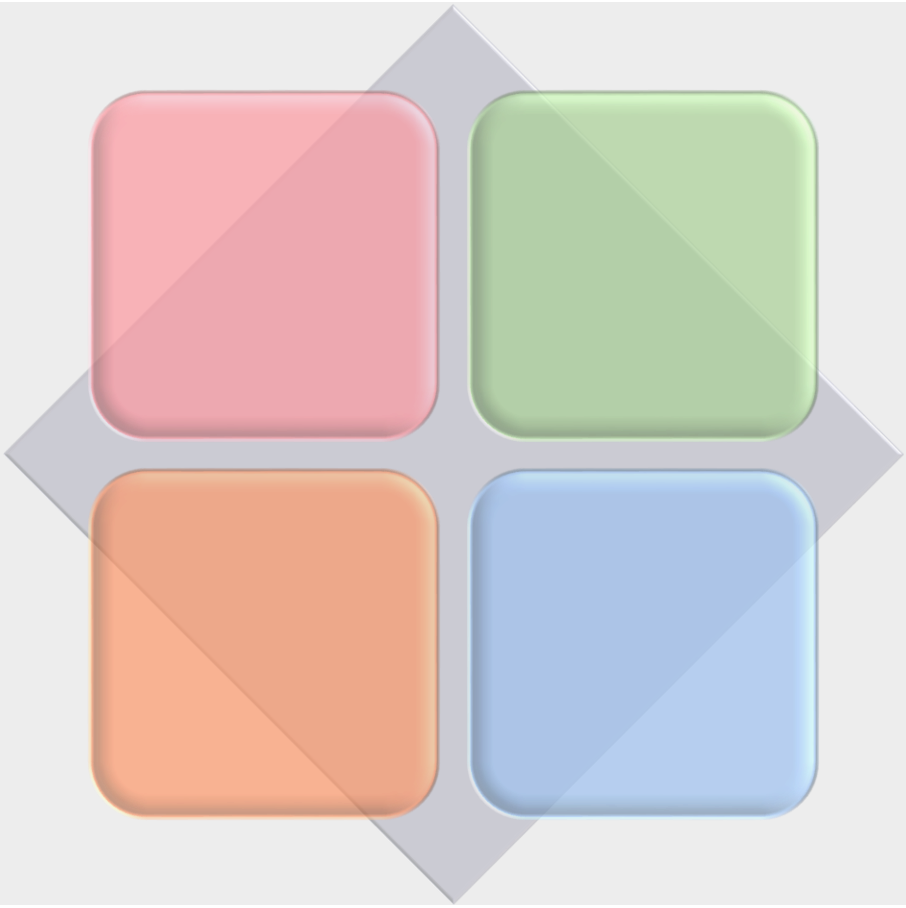

東 海 大 學 應 用 物 理 系

目錄

Influences of laser wavelength and intensity on perovskite solar cells

Guan-You Lin[1] and Forest Shih-Sen Chien[1,*]
[1]Department of Applied Physics, Tunghai University, Taiwan

Abstract

我們報告使用甲基碘化鉛（CH_3NH_3）PbI_3的納米顆粒（NPs）作為光收集器的固態介觀異質結太陽能電池。通過甲基碘化銨與PbI_2的反應生成鈣鈦礦納米顆粒，並沉積在亞微米厚度的介觀TiO_2薄膜上，上面覆蓋spiro-OMeTAD。我們有兩個不同TiO_2層的太陽能電池。一個是原始TiO_2，另一個是摻雜了Zn的TiO_2。

Perovskite solar cells

Photovoltaic Performance of two different perovskite solar cells

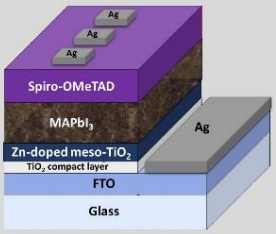

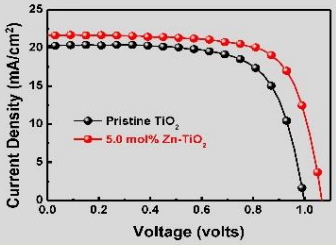

Pristine TiO_2	5.0 mol% Zn-TiO_2
V_{oc}: 1.00 V	V_{oc}: 1.07 V
J_{sc}: 20.30 mA/cm²	J_{sc}: 21.66 mA/cm²
FF: 69.4%	*FF*: 71.7%
PCE: 14.05%	*PCE*: 16.56%

Results and Discussion

Laser choosing

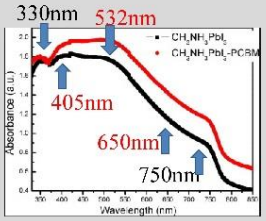

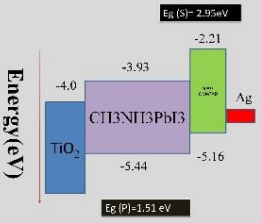

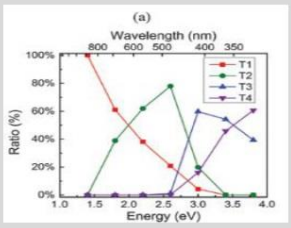

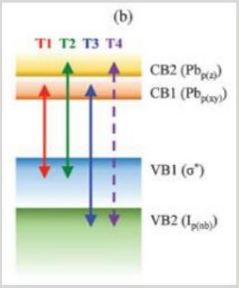

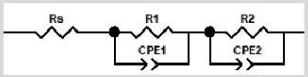

- 根據鈣鈦礦的吸收光譜我們選擇405nm，532nm，並以650nm代替750nm雷射作為註入光源

$$R^{-1}=G\propto\alpha\eta\frac{1}{\tau}P^{a}$$

R：resistance
G：recombination rate
α：absorption
η：efficiency
τ：life time
P：power
a：constant

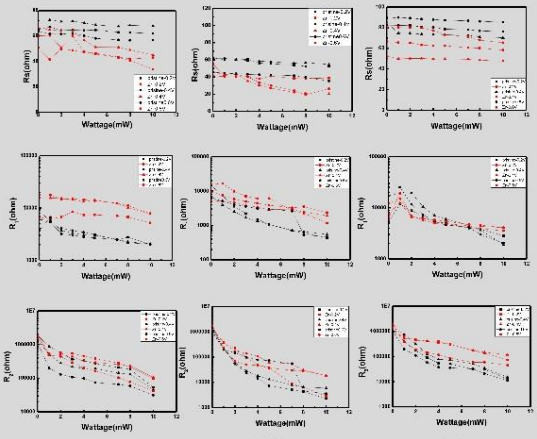

405nm laser　532nm laser　650nm laser
電阻比較

Conclusion

1. 隨著光照強度的增加，電阻一和電阻二皆會減少。
2. 考慮吸收值和狀態，複合率：532nm雷射> 405nm雷射> 650nm雷射。
3. EIS數據清楚地顯示了Zn摻雜納米棒中改進的電子傳輸和減少的重組。該結果表明Zn摻雜可以提高太陽能電池中的電子收集效率。

References

1. J. Mater. Chem. A, 2014,2, 19616,Mengjin Yang,[a] Kamal Kadel,[a]Yunyan Liu,[a]Kevin O'Shea,[b]Richaird Bone,[a]Xuewen Wang,[a]Jin IIe[a] and Whenzhi Li*[a]
2. :J.Mater. Chem. C,2016, 4, 5248, Hsin-An Chen,a Ming-Hsien Leeb and Chun-Wei Chen*ac

Anisotropic magnetoresistance in Ta/NiCo/Ta nanocrystalline thin films With different textures

P.F. Su[1](蘇品方), C.R. Wang[1](王昌仁), H.W. Chang[2](張晃暐)

[1]*Department of Applied Physics, Tunghai University, Taichung 407, Taiwan*
[2]Department of Physics, National Chung Cheng University , Chia-Yi, 621 Taiwan

Introduction

- The anisotropic magnetoresistance (AMR) of ferromagnetic alloys have attracted considerable attention for both the basic interest and technological applications in recent years.
- So far, the most commonly used permolly alloy material is NiFe.
- NiCo alloy has high anisotropic magnetoresistance (AMR) of 5%, but NiCo alloy also has high coecevity, so few report related to NiCo in thin films form is available.
- In this work, we investigate structure and MR properties of sputter-prepared Ta/$Ni_{80}Co_{20}$/Ta films through proper post-annealing.

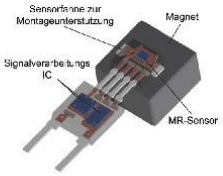

Experiment

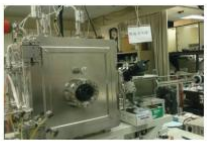

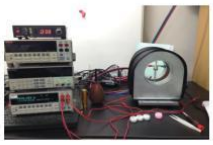

Crystal structures by XRD

MR ratio by 4-point probe method

Surface morphology by AFM

M-H curves by VSM

Ta(3nm)

$Ni_{100-x}Co_x$(20nm,0≤x≤15)

Ta(3nm)

SiO_2/Si(100)

Results and Discussion

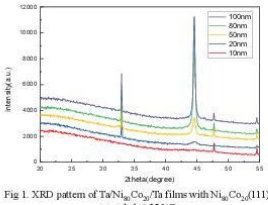

Fig 1. XRD pattern of Ta/$Ni_{80}Co_{20}$/Ta films with $Ni_{80}Co_{20}$(111) annealed at 250°C

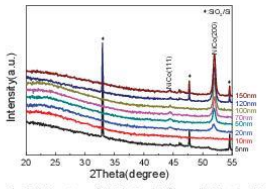

Fig 2. XRD pattern of Ta/$Ni_{80}Co_{20}$/Ta films with $Ni_{80}Co_{20}$(200) annealed at 250°C

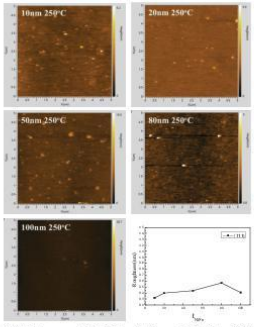

Fig 3. AFM images of Ta/$Ni_{80}Co_{20}$/Ta films with $Ni_{80}Co_{20}$(111) annealed at 250°C

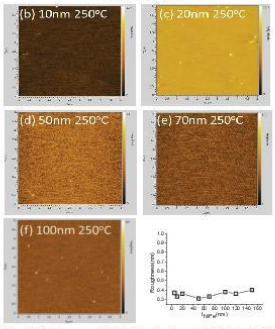

Fig 4. AFM images of Ta/$Ni_{80}Co_{20}$/Ta films with $Ni_{80}Co_{20}$(200) annealed at 250°C

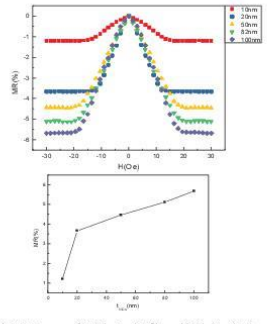

Fig 5. MR curves of Ta/$Ni_{80}Co_{20}$/Ta films with $Ni_{80}Co_{20}$(111) annealed at 250°C

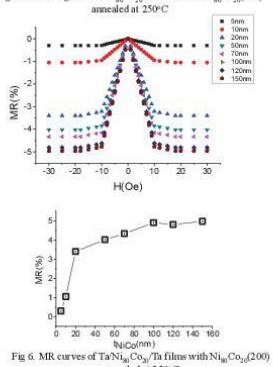

Fig 6. MR curves of Ta/$Ni_{80}Co_{20}$/Ta films with $Ni_{80}Co_{20}$(200) annealed at 250°C

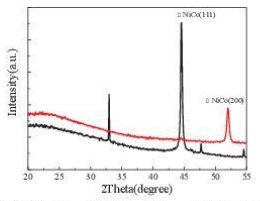

Fig 7. XRD pattern of Ta/$Ni_{80}Co_{20}$/Ta films with $Ni_{80}Co_{20}$(111) and $Ni_{80}Co_{20}$(200) annealed at 250°C

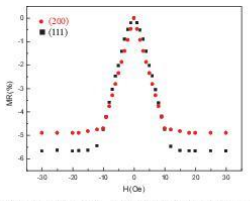

Fig 8. MR curves of Ta/$Ni_{80}Co_{20}$/Ta films with $Ni_{80}Co_{20}$(111) and $Ni_{80}Co_{20}$(200) annealed at 250°C

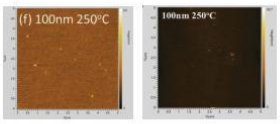

Fig 9. AFM images of Ta/$Ni_{80}Co_{20}$/Ta films with $Ni_{80}Co_{20}$(111) and $Ni_{80}Co_{20}$(200) annealed at 250°C

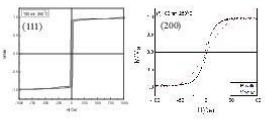

Fig 10. MH curves of Ta/$Ni_{80}Co_{20}$/Ta films with $Ni_{80}Co_{20}$(111) and $Ni_{80}Co_{20}$(200) annealed at 250°C

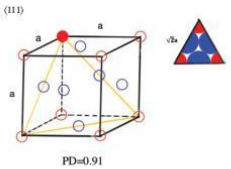

PD=0.91

Fig 11. Face density of fcc (111)

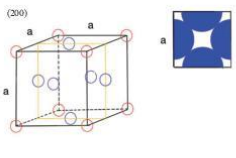

PD=0.74

Fig 12. Face density of fcc (200)

Conclusions

- Structure, magnetic properties and AMR of sputtered NiCo nanocrystalline films are studied.
- Nico(111) and (200) textures are successfully developed by tuning sputtering parameters and annealing temperature.
- The studied 2 series of films show good texture with flat surface, in-plane magnetic anisotropy, and high MR ratio.
- High Mr ratio of 5.6% and 5.0 % attained for NiCo(111) and NiCo(200), respectively, might be highly related to planar density of 0.91 and 0.74 for (111) and (200).

Texture and ferroelectric characterizations of $BiFeO_3$ thin films with $Co_{100-x}Pt_x$ underlayers

H.L. Chiang(江信綸), C.R. Wang(王昌仁), and H.W. Chang(張晃暐)
Department of Applied Physics, Tunghai University, Taiwan

Introduction

$BiFeO_3$ (BFO) has received much attentions due to potential applications in memory and advanced spintronic devices based on the electric-magnetic couplings. In order to facilitate these coupling, the use of ferromagnetic (FM) bottom electrode to induce a specific texture of BFO seems to be a most direct way. In this study, BFO films were grown on FM $Co_{100-x}Pt_x$ (111) underlayer(x=25~75) on glass and SiO_2/Si(100) substrate by sputtering. In addition to serving as a FM bottom electrode, $Co_{100-x}Pt_x$ (111) is also expected to reduce the formation temperature of BFO phase. A CoPt layer with optimized (111)-texture was used to grow high-quality BFO film.

Experiment

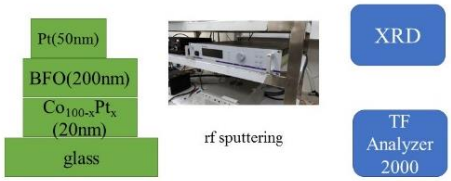

Result and disscussion

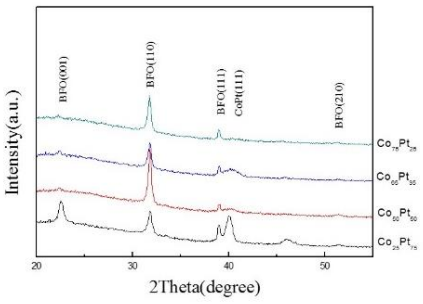

Fig 1. X-ray diffraction patterns of BFO/$Co_{100-x}Pt_x$/glass at 475℃

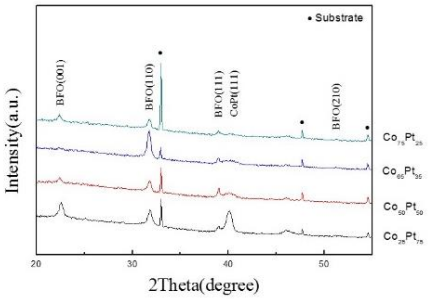

Fig 2. X-ray diffraction patterns of BFO/$Co_{100-x}Pt_x$/SiO_2 at 475℃

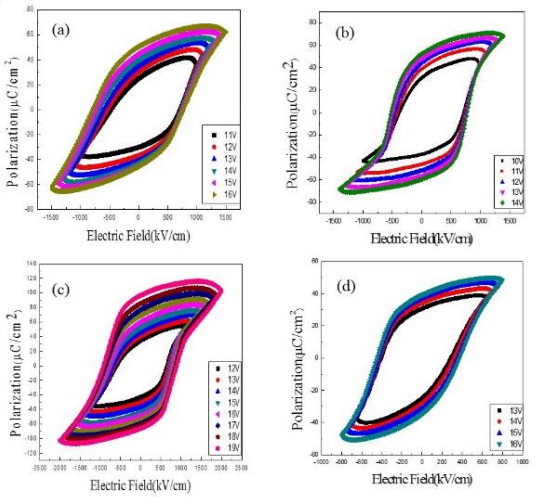

Fig 3. P-E curve of BFO/$Co_{100-x}Pt_x$/glass at 475℃
(a) $Co_{25}Pt_{75}$ (b) $Co_{50}Pt_{50}$ (c) $Co_{65}Pt_{35}$ (d) $Co_{75}Pt_{25}$

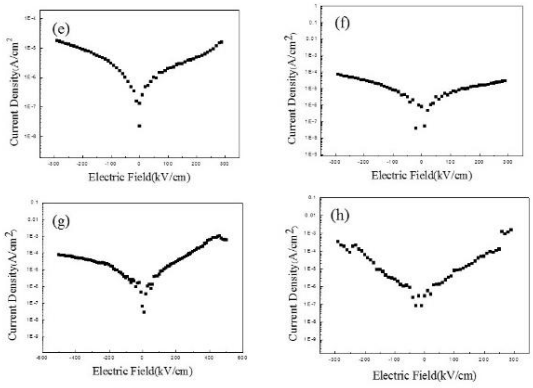

Fig 4. Leakage current of BFO/$Co_{100-x}Pt_x$/glass at 475℃
(a) $Co_{25}Pt_{75}$ (b) $Co_{50}Pt_{50}$ (c) $Co_{65}Pt_{35}$ (d) $Co_{75}Pt_{25}$

Conclusions

Using CoPt underlayer can reduce the growth temperature of BFO thin film with perovskite structure.

The structure of CoPt(111) can be tuned by $Co_{100-x}Pt_x$ and substrate temperature. BFO films grown on CoPt(111) underlayers exhibit a smooth surface and dense microstructure with small grain size.

Accordingly, CoPt underlayer not only as a bottom electrode but also enables BFO films possess ferroelectric behavior with good properties at low temperature of 475 ℃ due to low leakage current.

This study suggests an useful information to obtain BFO films with specific texture and also good ferroelectric properties.

Comparison on the microstructure and ferroelectric properties of $BiFeO_3$ polycrystalline films with various buffer layers

C.R. Huang(黃佳容), W.A. Chen(陳韋安), C.R. Wang[1](王昌仁), and H.W. Chang[2] (張晃暐)

[1]Department of Applied Physics, Tunghai University, Taichung 407, Taiwan
[2]Department of Physics, National Chung Cheng University, Chia-Yi 621, Taiwan

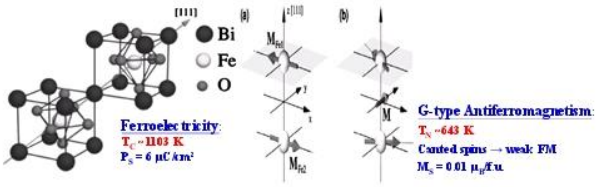

BFO as oxide ferroelectric films can be considered p-type semiconductors, which makes it possible to combine them with other n-type semiconductors in multifunctional epitaxial heterostructures.

In this study, we use ZnO and ITO because they are all n-type semiconductors. In this work, the structure of the polycrystalline thin film was studied, and the microstructure and ferroelectric properties were improved.

Experiment

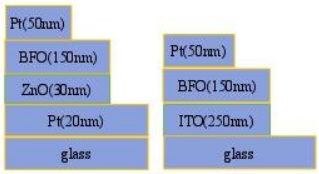

sputter

XRD → Crystal structure

SEM → Surface morphologies.

TF Analyzer 2000 → Ferroelectric properties.

Results and discussion

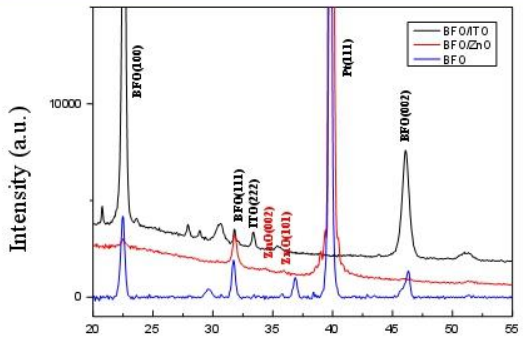

Fig1 X-ray diffraction patterns of BFO(150nm)/ZnO(30nm)/Pt/glass and BFO(150nm)/ITO(250nm)/glass and BFO/Pt.

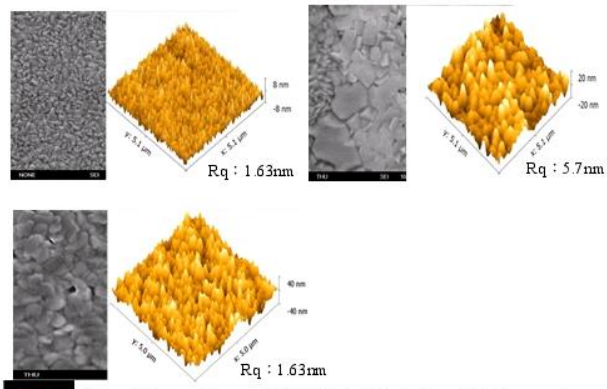

Fig2 SEM and AFM patterns of BFO(150nm)/ZnO(30nm)/Pt/glass and BFO(150nm)/ITO(250nm)/glass and BFO/Pt.

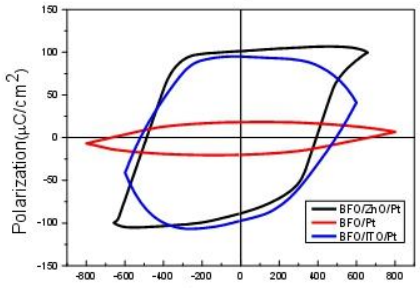

Fig3 P-E curve of BFO(150nm)/ZnO(30nm)/Pt/glass and BFO(150nm)/ITO(250nm)/glass and BFO/Pt.

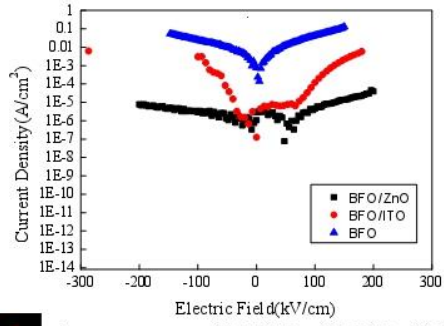

Fig5 Leakage current curve of BFO(150nm)/ZnO(30nm)/Pt/glass and BFO(150nm)/ITO(250nm)/glass and BFO/Pt.

Conclusions

- Microstructure and ferroelectric properties of sputtered BFO films on Pt, ITO, and ZnO buffer layers on the glass substrates are studied.
- The tetragonal structure with (001) texture is obtained for BFO on the Pt and ITO buffer layers, while (110) texture is found for ZnO one.
- ITO and ZnO could flatten the surface and interface of BFO layer, therefore reducing leakage and improving ferroelectric properties.
- BFO on ZnO exhibits better ferroelectric properties due to (110) texture, refined microstructure, and flattened surface.
- This study provides the important information to fabricate high quality BFO nanocrystalline film with texure and good ferroelectric properties.

Structure and Ferroelectric Properties of $BaTiO_3$ Polycrystalline Films on glass substrat

C.C. Kao[1], H.W. Chang[2]*, C.R. Wang[1]

[1]Department of Applied Physics, Tunghai University, Taichung 407, Taiwan
[2]Department of Physics, National Chung Cheng University, Chia-Yi 621, Taiwan

I. INTRODUCTION

- Perovskite $BaTiO_3$ (BTO) is one of the most important ferroelectric ceramic material (Tc~130°C) with a high piezoelectric constant and dielectric constant.
- BTO has a rich structural phase transition. From low to high temperature, there are crystal structures such as rhombohedra, orthorhombic, tetragonal and cubic.
- In addition to the cubic structure, BTO exhibits ferroelectric effect and is tetragonal at room temperature.

[illegible]	[illegible]	[illegible]
[illegible]	[illegible]	[illegible]
[illegible]	[illegible]	[illegible]

II. EXPERIMENT

200 nm BTO
Pt or FePt(001)
Glass

[illegible]

[illegible]

(a) [illegible] deposited at [illegible] °C

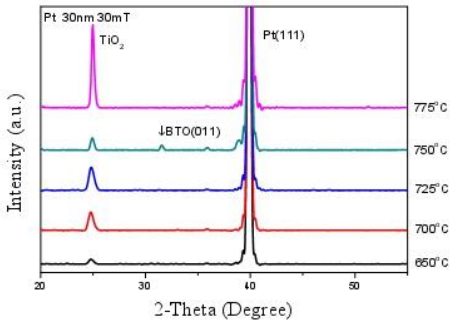

(b) BTO 750°C deposited under Oxygen pressure 30-100 mTorr

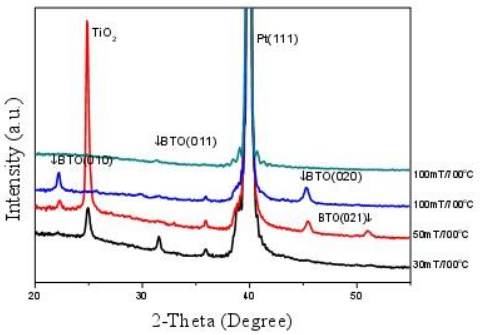

FIG. 1 (a) BTO thin films deposited at different temperature. (b) BTO thin films deposited under different pressure

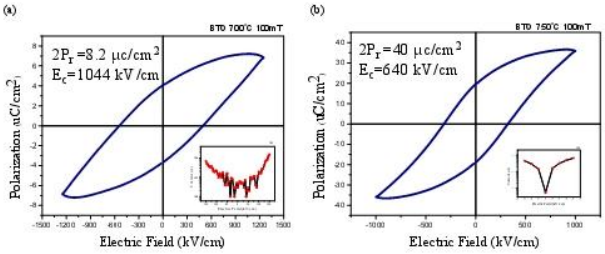

FIG. 2. (a) P-E loop of XRD of BTO films growth oxygen pressures of 100 mTorr at temperature 700°C. (b) P-E loop of XRD of BTO films growth oxygen pressures of 100 mTorr at temperature 750°C.

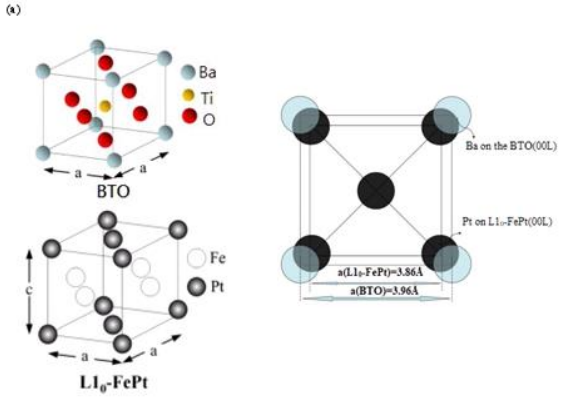

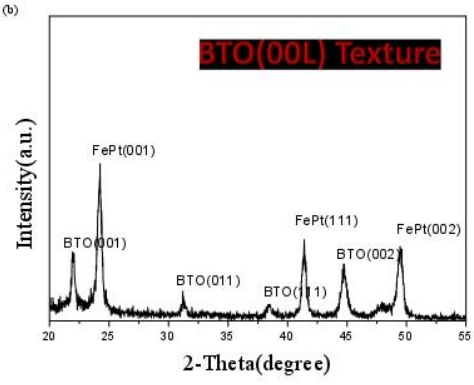

FIG. 3.(a) The structure diagram of BTO(001)/$L1_0$-FePt(001). (b) XRD of BTO/FePt.

IV. CONCLUSIONS

- The BTO films prepared by pulsed laser deposition on the glass substrates shows ferroelectric properties, $2P_r$= 40 μC/cm² at 750°C ⩽100 mTorr.
- Compared with BTO(001) and BTO(011) structures, BTO (001) has better ferroelectric properties.
- The selection of $L1_0$-FePt(001) as a bottom electrode is due to the similar lattice parameter between $L1_0$-FePt (a = 3.86 Å) and tetragonal BTO (a = 3.96 Å) trying to induce BTO (00*l*) texture growth.
- The structure of BTO(001)/ $L1_0$-FePt(001) is still in progress.

Structure, ferroelectric and magnetic properties of $Hf_{0.5}Zr_{0.5}O_2$ films on the glass substrates

W.S. Wang(王惟萱)[1], C.R. Wang(王昌仁)[1], H.W. Change(張晃暐)[2]

[1]Department of Applied Physics, Tunghai University, Taichung 407, Taiwan
[2]Department of Physics, National Chung Cheng University, Chia-Yi 621, Taiwan

Introduction

Ferroelectric behavior based on HfO_2-based films has been reported in recent years due to the ferroelectric phase stabilized by a variety of dopants.

Owing to processing simplicity and silicon compatibility, this has attracted attention promising for non-volatile memory applications. Most work has been devoted on the epitaxial $HfZrO_2$ films, but few study on the polycrystalline $(Hf,Zr)O_2$ films is available.

In this work, structure and ferroelectric properties of $Hf_{0.5}Zr_{0.5}O_2$ polycrystalline films with various oxygen pressures and substrate temperatures are studied.

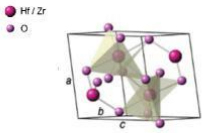

m-HZO

Experiment

Pulse Laser Deposition
Laser wavelength: 1064、532nm)

1064nm	1064、532nm
50nmPt	50nmPt
40nm HZO(T°C)	40nm HZO(x mTorr)
20nmPt	20nmPt
Glass	Glass

Crystal structures: XRD
Surface morphology: SEM
P-E Curve: TF analyzer 2000
M-H Curve: VSM

Result and discussion

HZO 40nm

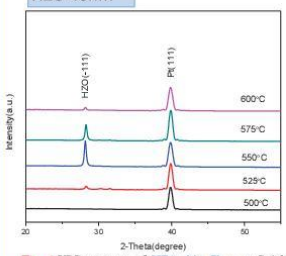

Fig. 1.XRD patterns of HZO thin films on Pt/glass substrate with oxygen pressures of 100mTorr at various temperatures of 500-600°C. (The wavelength of laser is 1064nm)

HZO 40nm

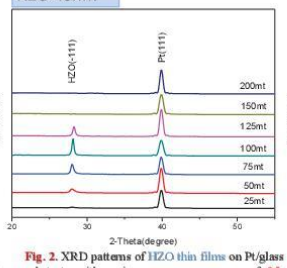

Fig. 2. XRD patterns of HZO thin films on Pt/glass substrate with various oxygen pressures of 25-200mt at temperature of 550°C. (The wavelength of laser is 1064nm)

HZO 30nm

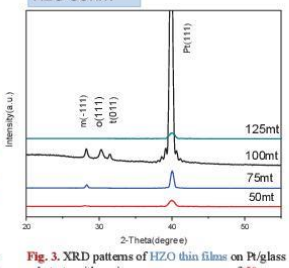

Fig. 3. XRD patterns of HZO thin films on Pt/glass substrate with various oxygen pressures of 50-125mt at temperature of 550°C. (The wavelength of laser is 532nm)

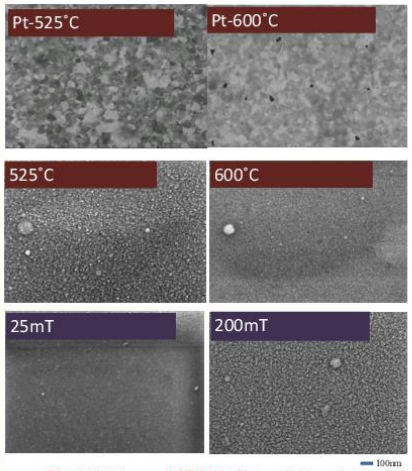

Fig. 4. SEM images of HZO thin films on Pt/glass substrate with oxygen pressures of 100mTorr at various temperatures of 525、600°C and the various oxygen pressures of 25、200mTorr at temperature 550°C.

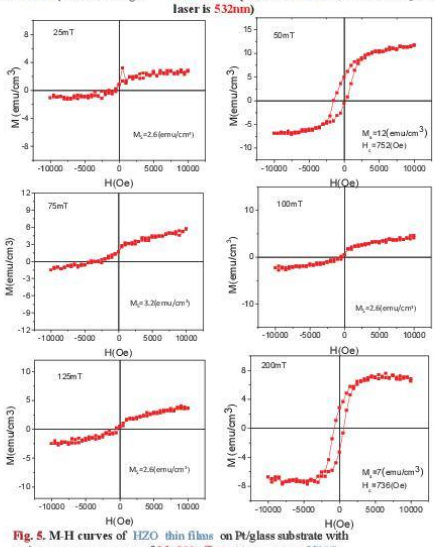

Fig. 5. M-H curves of HZO thin films on Pt/glass substrate with various oxygen pressures of 25~200mTorr at temperature 550°C.

550°C 75mT (The wavelength of laser is 1064nm)

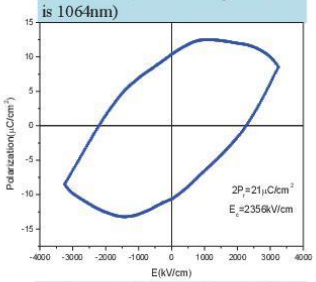

550°C 100mT (The wavelength of laser is 1064nm)

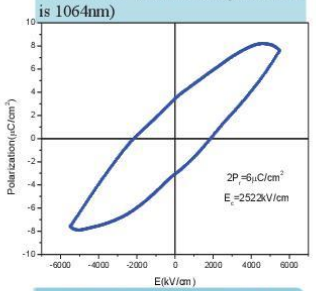

550°C 100mT(The wavelength of laser is 532nm)

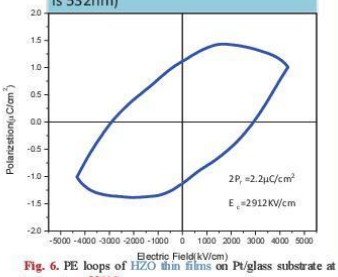

Fig. 6. PE loops of HZO thin films on Pt/glass substrate at temperature 550°C.

Conclusons

- A monoclinic ($\bar{1}11$) texture is detected for HZO films at 550 °C within oxygen pressure in the range of 50-125 mtorr and at 525-600 °C within oxygen pressure of 100 mtorr. A orthorhombic (111) and tetragonal (011) are coexisted for HZO films at laser wavelength of 532nm.
- Microstructure analysis show uniformly fine microstructure with small grain size is observed for all studied HZO films, and the size of HZO grains is increased from 10 nm at 525 °C to 25 nm at 600 °C.
- Ferromagnetic behavior found for the samples at the oxygen pressures in range of 25-200 mtorr is related to oxygen vacancies.
- A typical ferroelectric behavior with good properties is attained at 75 mtorr and 100 mtorr.

Preparation of TiO_2 nanoparticles by laser ablation in liquid

H. Lin, C.R. Wang
Department of Applied Physics, Tunghai University, Taichung, Taiwan

Introduction

- There are many researches that fabricating TiO_2 nanoparticle in liquid by chemistry way such as sol-gel method or some physical ways like SANSS or LAL. In this work, we checked what the properties of synthesized TiO_2 nanoparticles can be effected with the parameters on dashboard.
- This fabrication of nanoparticle is operating in liquid, so it's necessary to consider the light absorption efficiency of the liquid, and we used laser source with wavelength 1064nm.
- In this work, we investigated that the crystal phase or particle size of in-liquid-laser-process TiO_2 nanoparticles are different with different power percentage of laser.

Experimental session

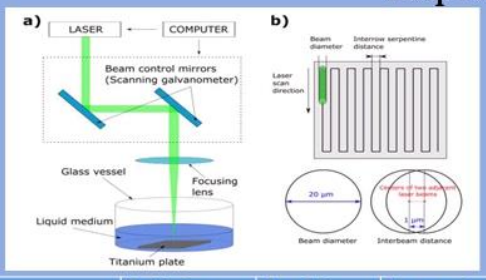

	Particle size	Phase shift	Concentration
Power of laser	No effect	Influential	Influential

Power parameter of laser in [illegible] is equal to [illegible]
The range of laser power was setting [illegible] to [illegible]

Particle size
Crystal phase
With TEM

[illegible]-existent reaction by metal ions & [illegible] exposure

Results & Discussion

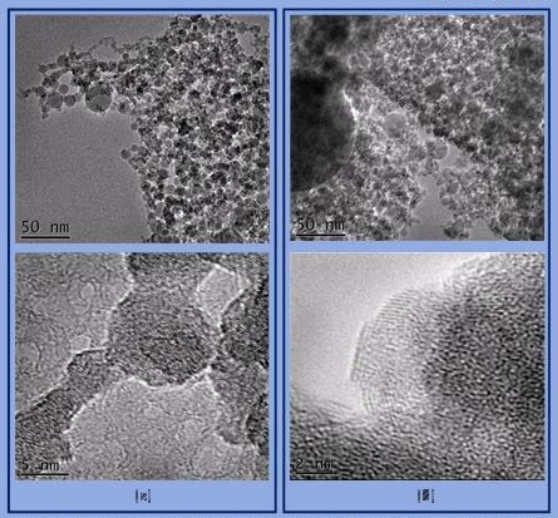

[a] [b]

TEM graphs of Ti oxide nanoparticles fabricated with LAL in different laser power (a) 100% (b) 50%

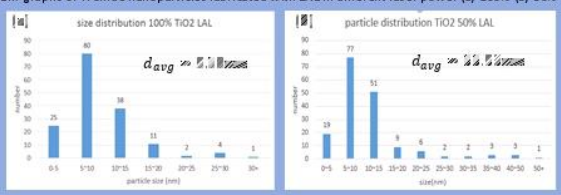

Particle size distribution of Ti oxide nanoparticles under different laser power [a] [illegible] [b] [illegible]

d(Å)	rutile	anatase	brookite	Ti_2O_3	Ti_3O_5
1.54			(600)'		
1.66		(211)'			
1.91		(200)'			
1.97			(411)'		
2.04					
2.09				(202)'	
2.12			(222)'		
2.16					
2.2	(111)'				
2.21				(113)'	
2.23					
2.36					
2.29	(200)'				
2.31		(112)'			
2.36		(004)'			
2.38					
2.4		(103)'			
2.46	(101)'				
2.55					
2.61					
2.67					(-203)
2.76					
2.8					
2.87					
2.92					
3.04					
3.29					(111)'
3.43					(-202)'
3.55		(101)'			
4.71					(002)'

d(Å)	rutile	anatase	brookite	Ti_2O_3
2.21	(111)'			
2.72				
2.4		(004)'		
2.48	(101)'			
1.97				
2.29	(200)'			
2.36		(004)'		
2.55				
2.8				
1.91		(200)'		
2.48	(101)'			
2.16				
2.74				
2.99				
2.42		(105)'		
2.24				(113)'
2.99				
2.48	(101)'			

[illegible] is mainly nanosize structure phase in [illegible].

We found that [illegible] fabrication has more crystalline phase than [illegible] fabrication.

[illegible] laser power [illegible] laser power

Future works:

- Find the condition fabricating phase-pure TiO_2 nanoparticles
- Qualitative measurement of concentration of TiO_2 nano-colloid, compare the photo-catalyst properties of TiO_2 nano-colloids with different concentration

Conclusions

Results reveal power-changing process can only produce TiO2 NPs with **particle size in certain range** and it won't only fabricate a **particular phase** but change the proportion of each phase in the process.
The laser power whose range was set from 20W to 10W, is so small, led to the produced Ti oxide nanoparticles with the main phase in rutile.

Exchange bias in Co/MnPt polycrystalline films on SiO_2/Si(100) substrates with Ta underlayer

Y.H. Chien[1], P.H. Pan[1], H.W. Chang[2]*, C.R. Wang[1]*, Lance Horng [3]
[1] Department of Applied Physics, Tunghai University, Taichung, 407 Taiwan.
[2] Department of Physics, National Chung Cheng University, Chia-Yi, 621 Taiwan
[3] Department of Physics, National Changhua University of Education, Changhua 500, Taiwan.

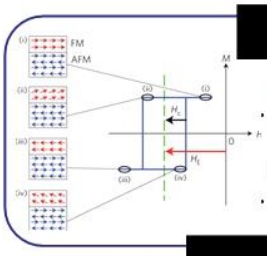

[redacted]ange bias systems, $L1_0$-MnPt exhibited high bolcking temperature and excellent corrosion resistance.

- In this study, Ta/Co/MnPt films are prepared on SiO_2/Si(100) substrates at room temperature (RT) by sputtering at the external magnetic field of 1 kOe induced NdFeB sintered magnets.
- The studied films are optimized by modification of thickness of Ta underlayer and MnPt.

[redacted]

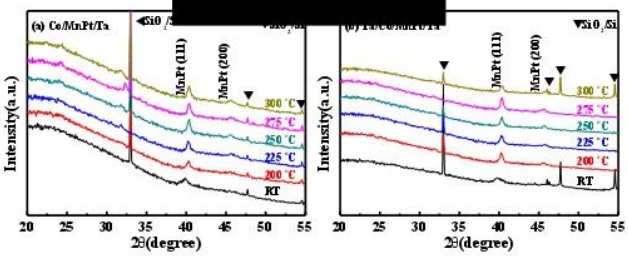

Fig.1. XRD patterns of Co/MnPt bilayer deposited on various Ta thickness (a) 0 nm and (b) 5 nm with various annealing temperature.

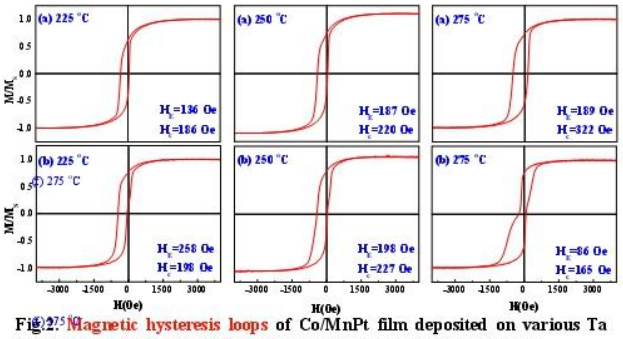

Fig.2. Magnetic hysteresis loops of Co/MnPt film deposited on various Ta thickness (a) 0 nm and (b) 5 nm with various annealing temperature.

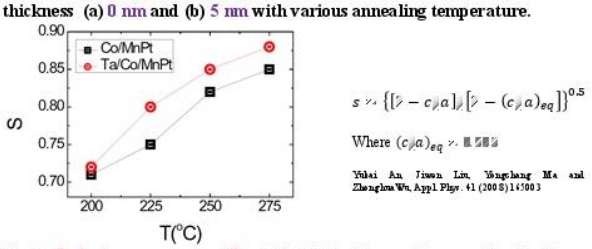

$$S = \{[P - c/a][P - (c/a)_{eq}]\}^{0.5}$$

Where $(c/a)_{eq} =$ [redacted]

Yubai An, Jiwen Liu, Yonghang Ma and Zhenghua Wu, Appl. Phys. 41 (2008) 145003

Fig.3. Ordering parameter (S) of Co/MnPt films without and with 5-nm-thick Ta underlayer annealed at various temperatures in the range of 225–275 °C.

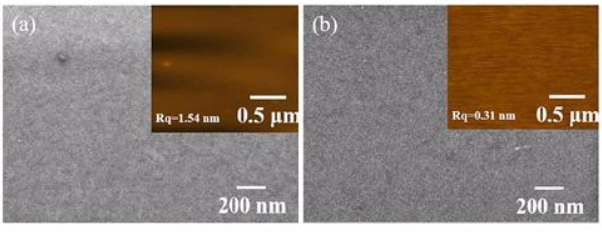

Fig. 4. AFM and SEM images of annealing temperature 225 °C with various thickness of Ta underlayer (a) 0 nm and (b) 5 nm

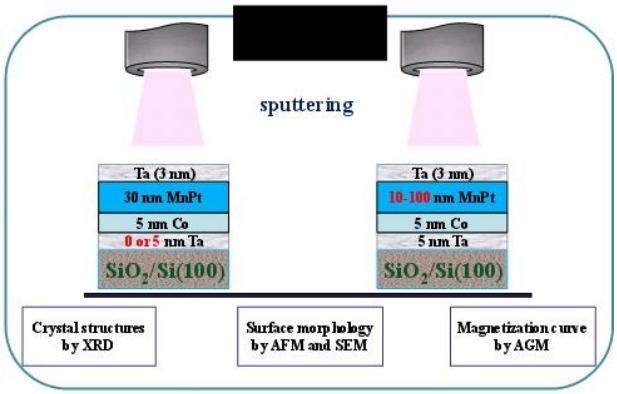

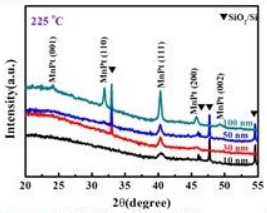

Fig.4. XRD patterns of Ta/Co/MnPt film annealed at 225 °C with various MnPt thicknesses.

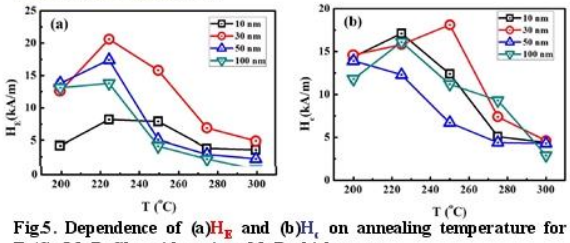

Fig.5. Dependence of (a)H_E and (b)H_c on annealing temperature for Ta/Co/MnPt film with various MnPt thicknesses.

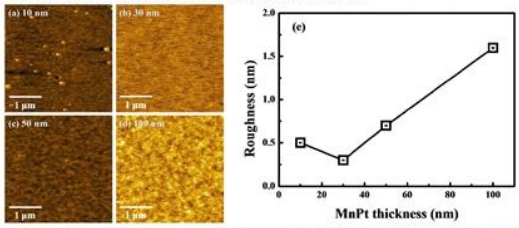

Fig.6. (a)–(d) AFM images of the studied films with various MnPt thickness annealed at 275 °C and (e) dependence of roughness on MnPt thickness for Ta/Co/MnPt films annealed at 225–275 °C.

[redacted]

- The largest H_{eb} of 258 Oe [redacted] the presented Ta/Co/MnPt(30 nm) films by sputtering at the external magnetic field with 5 nm thickness of Ta underlayer and 275 °C of annealing temperature, and it accompanies a small H_c of 198 Oe.
- Flatter surface of Co/MnPt deposited on Ta underlayer is obtained.
- The strengthened diffraction intensity of MnPt (111) and the presence other diffraction peaks with MnPt thickness reveal enhanced $L1_0$-ordering in MnPt layer.
- Larger H_c than H_E obtained in 10-nm-thick MnPt results from larger exchange interaction energy between the Co and MnPt than anisotropy energy of MnPt.
- This study provides useful information to fabricate exchange bias Co/MnPt system.

Magnetic properties of MnPt/Co films on glass substrates

Y.C. Chen[1], H.W. Chang[2], C.R. Wang[1], Lance Horng[3]

[1] Department of Applied Physics, Tunghai University, Taichung, 407 Taiwan.
[2] Department of Physics, National Chung Cheng University, Chia-Yi, 621 Taiwan
[3] Department of Physics, National Changhua University of Education, Changhua 500, Taiwan.

Introduction

MnPt, an antiferromagnetic (AF) intermetallic alloy with a very high Néel temperature T_N ~ 973 K, has attracted much attention due to the potential applications in sensors, magnetic random access memory (MRAMs), read heads, and advanced spintronic devices.

In this study, Ta/MnPt/Co films are prepared on glass substrates at room temperature (RT) by sputtering. The samples are annealed at designated temperature, and then cooling to RT at the applied magnetic field of 2 kOe. Ta underlayer effect on microstructure and magnetic properties of MnPt/Co are studied.

Experiment

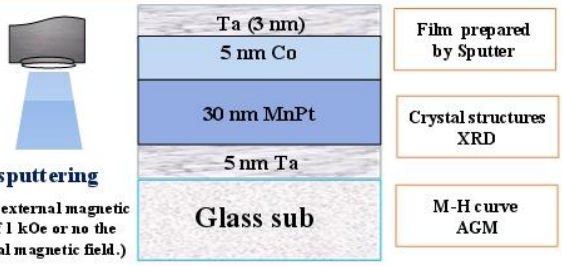

Results and discussion

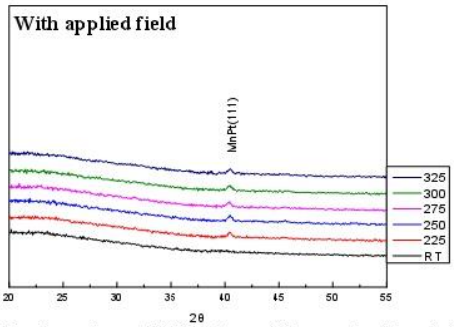

Fig1. X-ray diffraction patterns of XRD patterns of the sample with applied field glass/Ta(3)/MnPt(30)/Co(5)/Ta(3) annealed at designated temperature for 1hr.

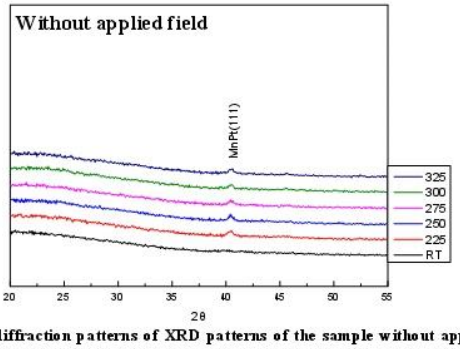

Fig2. X-ray diffraction patterns of XRD patterns of the sample without applied field glass/Ta(3)/MnPt(30)/Co(5)/Ta(3) annealed at designated temperature for 1hr.

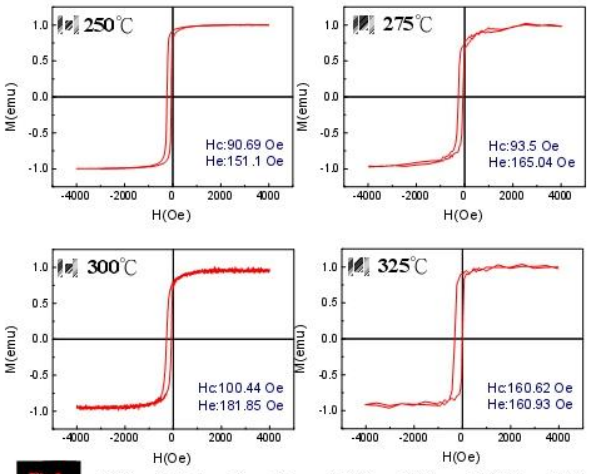

Fig3. M-H loops of the sample with applied field glass/Ta(5nm)/MnPt(30nm)/Co(5nm) annealed at (a) 250°C (b) 275°C (c) 300 °C ; (d) 325 °C for 1hr.

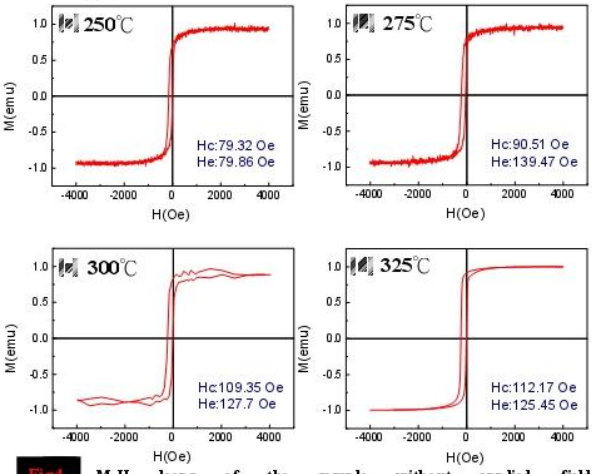

Fig4. M-H loops of the sample without applied field glass/Ta(5nm)/MnPt(30nm)/Co(5nm) annealed at (a) 250°C (b) 275°C (c) 300 °C ; (d) 325 °C for 1hr.

Conclusions

- **Magnetic properties of the sample with applied field and the sample without applied field systems annealed at various temperatures are studied.**
- **At the same annealing temperature, the exchange bias (H_{ex}) of samples with applied field is always lager than the samples without applied field.**
- **This study provides useful information to optimized MnPt-based exchange bias system.**

Structure and ferroelectric properties of $BiFeO_3$ films with CoPt/Pt buffer layer on glass substrates

M.L. Chen(陳孟霖)[1], C.R. Wang(王昌仁)[1] and H.W. Chang(張晃暐)[2]

[1]Department of Applied Physics, Tunghai University, Taichung 407, Taiwan

[2]Department of Physics, National Chung Cheng University, Chia-Yi 622, Taiwan

Introduction

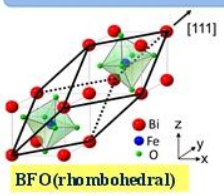

BFO(rhombohedral)

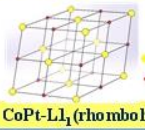

CoPt-Ll_1(rhombohedral)

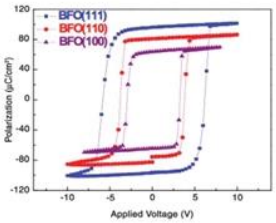

Ferroelectric properties of the textures for BFO epitaxial films.

Experiment

sputter

XRD → Crystal structures.

SEM → Surface morphology.

TF Analyzer 2000 → Ferroelectric properties.

Results and discussion

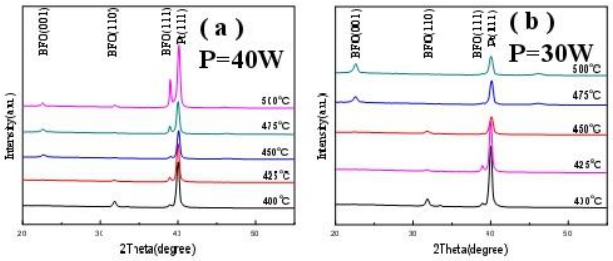

Fig1. XRD patterns of BFO(150 nm)/CoPt (5 nm)/Pt(20 nm/glass at (a)P=40W and (b)P=30W deposited at different temperatures.

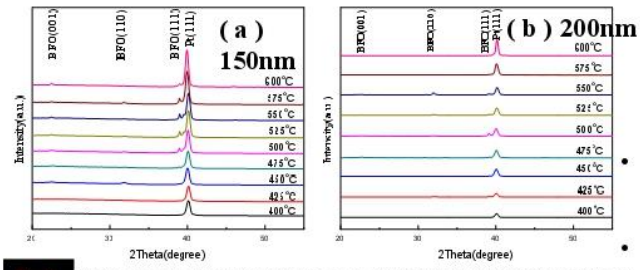

Fig2. XRD patterns of BFO(a)150 nm, and (b)200 nm/CoPt (5 nm)/Pt(20 nm)/glass at P=20 W deposited at different temperatures.

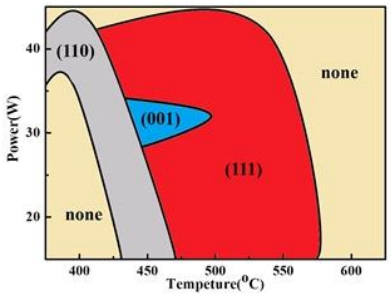

Fig3. Phase diagram of the textures for this studies 150 nm-thick BFO films.

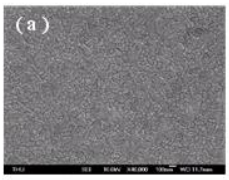

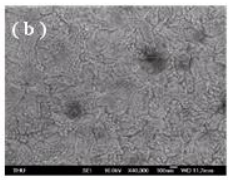

Fig4. SEM images of BFO films on CoPt(5nm)/Pt(20nm)/at (a)P=40W and (b)P=30W different temperature at 400°C.

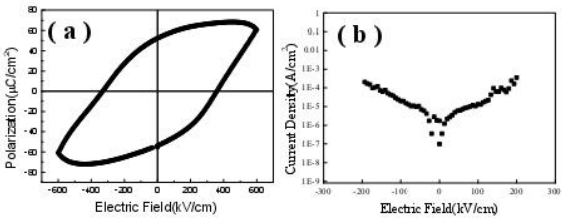

Fig5. (a)P-E curves and (b)J-V loops of BFO(150nm)/ CoPt(5nm)/Pt(20nm)/40W at 450°C.

Conclusions

- **Textures of BFO films can be controlled by sputtering parameters and deposition temperature: (111) at P=40W and T=475-500 °C and P=20W and T=475-575 °C; (110) at P=40W and T=400 °C and P=30W and T=425-450 °C; (001) at P=30W and T=475-500 °C, respectively.**
- **Low deposition temperature results in dense microstructure and low leakage.**
- **As a result, good ferroelectric properties can be obtained.**

Improved perpendicular magnetic properties of pulsed-dc-sputtered FePt thin films

D.Y. Lin[1], P.Y. Yeh[1], C.Y. Shen[2], H.W. Chang[3*], M.Y. Lee[1], C.R. Wang[1]

[1]*Department of Applied Physics, Tunghai University, Taichung, 407 Taiwan*

[2]*Department of Electrical Engineering, Hsiuping University of Science and Technology, Taichung, Taiwan*

[3]*Department of Physics, National Chung Cheng University, Chia-Yi, 621 Taiwan*

Introduction

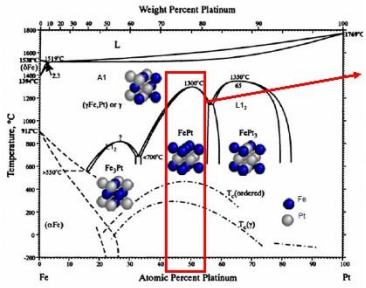

$L1_0$ FePt Advantage :

1. *high K_u~$7x10^7$ (erg/cm^3)*
2. *nice T_c (~450 °C)*
3. *large M_s(13.8 kG)*
4. *good chemical stability*

Applications of FePt alloy :

Microscopic state

Film, particles

micro-electro-mechanical systems (MEMS)

Rare report on FePt films prepared by pulsed direct current sputtering is available, in this work, magnetic properties, structure, and microstructure of FePt films prepared by pulsed dc sputtering are studied. Magnetic properties and structure of the films prepared by dc and pulsed dc sputtering are also compared.

Experiment

	dc	Pulse dc
Thickness	30 nm	30 nm
Annealing	300-700 °C	300-700 °C
Pulse frequency(PF)	-	35 kHz
Pulse duration(PD)	-	50%

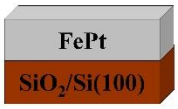

XRD *Structure* | VSM *Magnetic properties* | MFM *Magnetic domain* | TEM *Microstructure*

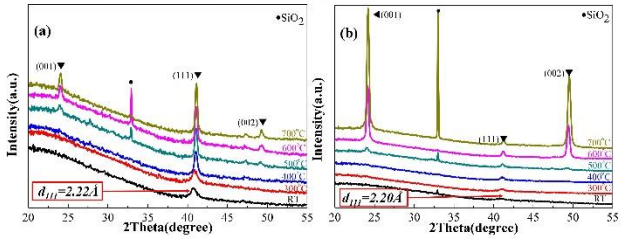

Fig.1 XRD patterns for the FePt films prepared by (a) dc sputtering and (b) pulsed dc sputtering followed by post-annealing at 300-700 °C.

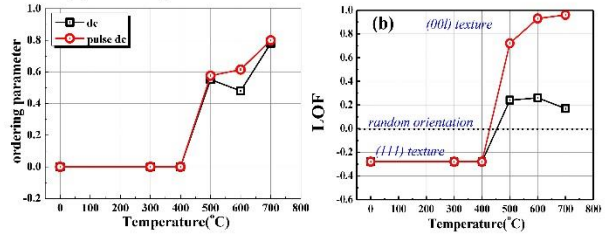

Fig.2 Dependence of ordering parameter and LOF on annealing temperature for the dc and pulsed dc sputtered FePt thin films.

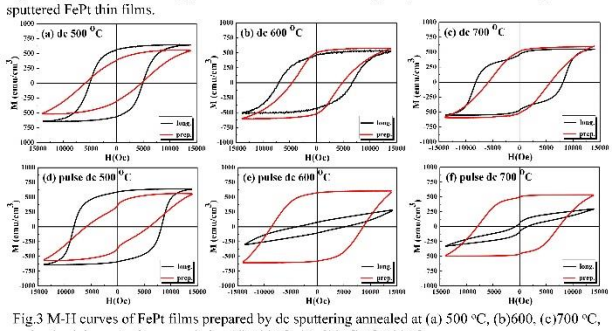

Fig.3 M-H curves of FePt films prepared by dc sputtering annealed at (a) 500 °C, (b)600, (c)700 °C, and pulsed dc sputtering annealed at (d) 500 °C, (e) 600 °C, (f) 700 °C.

Results and Discussion

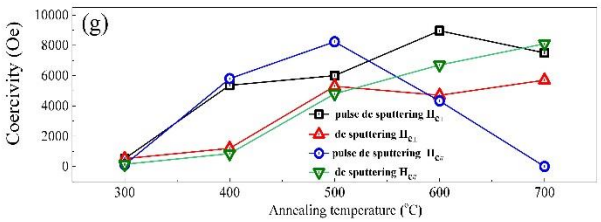

Fig.3 (g) Comparison on coercivity of FePt films prepared by dc and pulsed dc sputtering and post annealed at 300-700 °C.

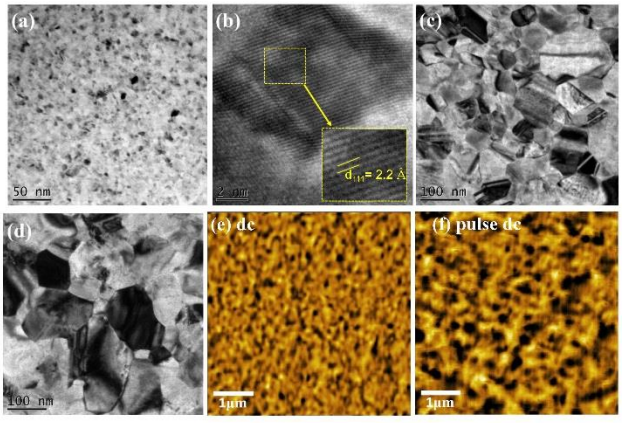

Fig.4 TEM images for the FePt films prepared by pulse dc sputtering (a),(b) as-deposition, and (c) dc sputtering followed by post-annealed at 700 °C, and (d) pulse dc sputtering and post-annealing at 700 °C. MFM images for the FePt films prepared by (c) dc sputtering and (f) pulsed dc sputtering followed by post-annealing at 700 °C.

Conclusions

- **Comparing to conventional straight dc sputtering, the films prepared by pulse dc sputtering have a 100 °C lower onset temperature of ordering, higher ordering parameter, well developed (001) texture, and remarkable perpendicular magnetic anisotropy.**
- **The as deposited film prepared by pulse dc sputtering was identified having a higher tensile strain in in-plane direction, which is considered as an assistance for the development of (001) texture.**
- **The results of this study suggest pulse dc sputtering as an effective approach to prepare high quality FePt thin films with strong perpendicular magnetic anisotropy.**

N-body simulation by Barnes-Hut algorithm

Shao-Fu Liu (劉少輔) , Kwai-Kong Ng (吳桂光)
Department of Applied Physics, Tunghai University, Taichung, Taiwan R.O.C

Abstract Simulating systems of many bodies, like interacting galaxies, can be a very difficult task due to the limitation of computer power. In general, calculating forces between bodies in an N-body system requires $O(N^2)$ operations and simulating a massive n-body system of 10^{10} bodies becomes impractical. Therefore different hierarchical methods are being developed to tackle this difficulty. One of these hierarchical methods that requires O(NlogN) operations is the Barnes-Hut algorithm, which is the method employed in this study. The crucial idea in speeding up the brute force n-body algorithm is to group nearby bodies and approximate them as a single body. If the group is sufficiently far away, we can approximate its gravitational effect by considering its center of mass alone.

Constructing tree structure

The Barnes-Hut algorithm use an quad-tree structure to group bodies that are sufficiently nearby. Bodies are divided into quadrants recursively, as shown in the figure, and are assigned to the nodes of a tree structure as the following procedure:

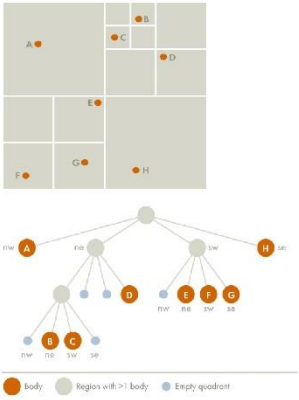

1. If node x does not contain a body, put the new body b here.
2. If node x is an internal node, update the center-of-mass and total mass of x. Recursively insert the body b in the appropriate quadrant.
3. If node x is an external node, then there are two bodies b and c in the same region. Subdivide the region further by creating four children.
4. Then, recursively insert both b and c into the appropriate quadrant(s). Since b and c may still end up in the same quadrant, there may be several subdivisions during a single insertion.
5. Finally, update the center-of-mass and total mass of x.

Calculating the net force

To calculating the net gravitational force acting on each body, we need the following recursive procedures starting with the root of the quad tree. Assuming that we want to calculate the net force acting an body *B*.

The force calculation use the Newton's law of universal gravitation :

$$\vec{F} = \sum_i \hat{r} \frac{G m_B m_i}{r_{iB}^2}$$

1. If the current node is an external node(it is not body *B*), calculate the force exerted by the current node on *B*, and add this amount to *B*'s net force.
2. Otherwise, calculate the ratio ***S / D***. If ***S / D*** < **θ**, treat this internal node as a single body, and calculate the force it exerts on body *B*, and add this amount to *B*'s net force (***S*** represents the quadrant side of length. ***D*** represents the distance from the body B to the center of mass for the root cell. **θ** represents the accuracy of the simulation.)
3. Otherwise, run the procedure recursively on each of the current node's children.

Time evolution

Given a body's net force, we can use the Newton's 2rd law to compute the acceleration of the body.
The ordinary differential equations are solved numerically by using the standard Runge–Kutta methods.

Then update the body's data and build new quad-tree, calculate the net force, solve the ODE, and run the procedure recursively .

Three stars system simulation

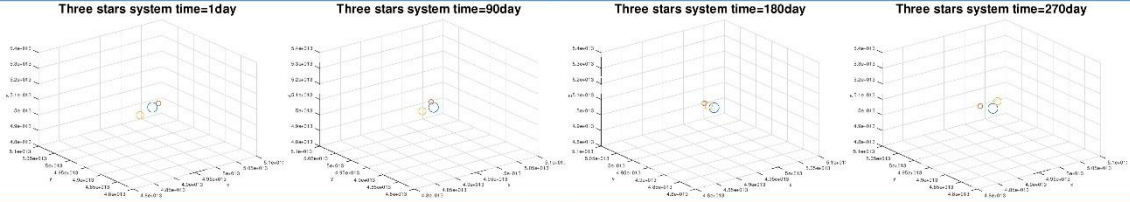

Reference

[1] Horellou. D. C., Bjerkeli. P., (2007). *N-body simulations of interacting galaxies* (Master's thesis, Chalmers University of Technology). Retrieved from https://research.chalmers.se/en/person/gu97pebj
[2] 戴宗元、蔡美琴、吳麗芬(民76)。*演算法與資料結構*。臺北市：儒林。
[3] T. Ventimiglia., K. Wayne., (2003). *Barnes-Hut Galaxy Simulator.* Retrieved from http://arborjs.org/docs/barnes-hut (2003).

Optical Filters Based on Silver Nanoslits Embedded with Liquid Crystals

Yu-Hsuan Tsai[1*], Li-Yu Wu[1], Kuang-Li Lee[2], Pei-Kuen Wei[2], Chia-Yi Huang[1]

[1]Department of Applied Physics, Tunghai University, Taichung, Taiwan
[2]Applied Sciences, Research Center, Taipei, Taiwan
* presenting author:Yu-Hsuan Tsai, email:tstina0512@gmail.com

Abstract

The optical properties of the silver slits arise from surface plasma resonance (SPR), and the resonance frequency of the slits depends on the refractive indices of their surrounding media. The resonance wavelength of the test sample returns to its initial state after the removal of the voltages, so the tuning of the resonance wavelength is reversible. The experimental results depict that the silver slits embedded with the liquid crystal (LC) cell can be used to develop visible-light filters.

Fabrication

Interpret nanoslits on plastic substrate by hot pressing technique

Metallic film with a thickness of 120 nm is deposited on the plastic substrate

An empty cell comprises the substrate and an ITO glass on which a homogeneous aligned layer is coated. The empty cell is filled with LC

Application of voltages to an LC cell changes the refractive index of the LC. The spectrum of the nanoslits is blueshifted as visible light irradiates on the nanoslits. Therefore, the LC cell can be used to develop visible-light filters.

Experiment

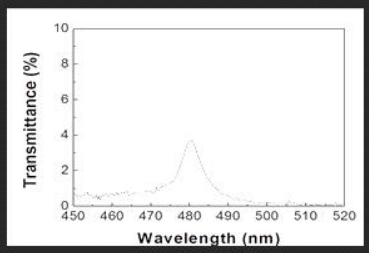

- Spectrum of LC cell with nanoslits whose period ($\Lambda_{400\,nm}$) is 400 nm

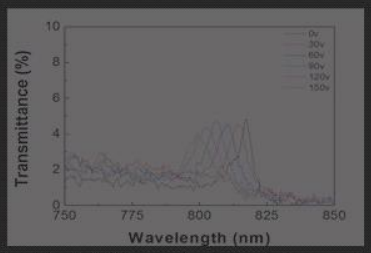

- The spectral blueshift arises from the fact that the LC director is oriented in a direction perpendicular to the substrate at 150 V.
- The spectrum of the LC cell with the silver nanoslits is reversible at the applied voltages

Spectra of LC cell with silver nanoslits whose period is $\Lambda_{400\,nm}$ at various applied voltages.

Theory

✓ Surface plasmon resonance, SPR

According to the Maxwell Equation, only the TM wave magnetic mode (TM mode) can produce the SPR solution.

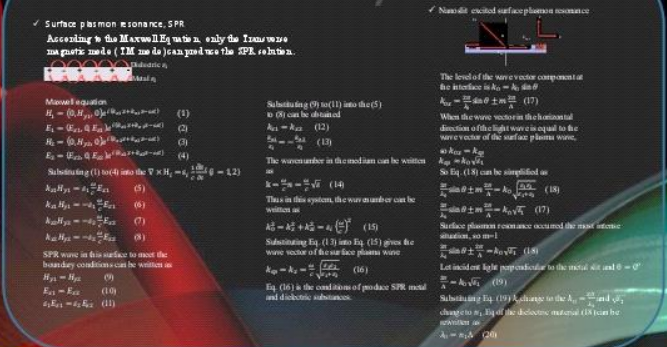

Maxwell equation

$$H_1 = (0, H_{y1}, 0)e^{i(k_{x1}x+k_{z1}z-\omega t)} \quad (1)$$
$$E_1 = (E_{x1}, 0, E_{z1})e^{i(k_{x1}x+k_{z1}z-\omega t)} \quad (2)$$
$$H_2 = (0, H_{y2}, 0)e^{i(k_{x2}x+k_{z2}z-\omega t)} \quad (3)$$
$$E_2 = (E_{x2}, 0, E_{z2})e^{i(k_{x2}x+k_{z2}z-\omega t)} \quad (4)$$

Substituting (1) to (4) into the $\nabla \times H_i = \varepsilon_i \frac{1}{c}\frac{\partial E_i}{\partial t}$ ($i = 1,2$)

$$k_{z1}H_{y1} = \varepsilon_1 \frac{\omega}{c}E_{x1} \quad (5)$$
$$k_{x1}H_{y1} = -\varepsilon_1 \frac{\omega}{c}E_{z1} \quad (6)$$
$$k_{z2}H_{y2} = -\varepsilon_2 \frac{\omega}{c}E_{x2} \quad (7)$$
$$k_{x2}H_{y2} = -\varepsilon_2 \frac{\omega}{c}E_{z2} \quad (8)$$

SPR wave in this surface to meet the boundary conditions can be written as

$$H_{y1} = H_{y2} \quad (9)$$
$$E_{x1} = E_{x2} \quad (10)$$
$$\varepsilon_1 E_{z1} = \varepsilon_2 E_{z2} \quad (11)$$

Substituting (9) to (11) into the (5) to (8) can be obtained

$$k_{z1} = k_{z2} \quad (12)$$
$$\frac{k_{x1}}{\varepsilon_1} = -\frac{k_{x2}}{\varepsilon_2} \quad (13)$$

The wavenumber in the medium can be written as

$$k = \frac{\omega}{c}n = \frac{\omega}{c}\sqrt{\varepsilon} \quad (14)$$

Thus in this system, the wavenumber can be written as

$$k_{sp}^2 = k_x^2 + k_z^2 = \varepsilon_i \left(\frac{\omega}{c}\right)^2 \quad (15)$$

Substituting Eq. (13) into Eq. (15) gives the wave vector of the surface plasma wave

$$k_{sp} = k_x = \frac{\omega}{c}\sqrt{\frac{\varepsilon_1\varepsilon_2}{\varepsilon_1+\varepsilon_2}} \quad (16)$$

Eq. (16) is the conditions of produce SPR metal and dielectric substances.

✓ Nanoslit excited surface plasmon resonance

The level of the wave vector component at the interface is $k_{ix} = k_0 \sin\theta$

$$k_{sp} = \frac{2\pi}{\lambda}\sin\theta \pm m\frac{2\pi}{\Lambda} \quad (17)$$

When the wave vector in the horizontal direction of the light wave is equal to the wave vector of the surface plasma wave, so $k_{sp} = k_{ix}$

$$k_{sp} = k_0\sqrt{\varepsilon_1}$$

So Eq. (18) can be simplified as

$$\frac{2\pi}{\lambda}\sin\theta \pm m\frac{2\pi}{\Lambda} = k_0\sqrt{\frac{\varepsilon_1\varepsilon_2}{\varepsilon_1+\varepsilon_2}} \quad (18)$$

$$\frac{2\pi}{\lambda}\sin\theta \pm m\frac{2\pi}{\Lambda} = k_0\sqrt{\varepsilon_1} \quad (17)$$

Surface plasmon resonance occurred the most intense situation, so m=1

$$\frac{2\pi}{\lambda}\sin\theta \pm \frac{2\pi}{\Lambda} = k_0\sqrt{\varepsilon_1} \quad (18)$$

Let incident light perpendicular to the metal slit and $\theta = 0°$

$$\frac{2\pi}{\Lambda} = k_0\sqrt{\varepsilon_1} \quad (19)$$

Substituting Eq. (19) λ_0 change to the $\lambda_0 = \frac{2\pi}{k_0}$ and $\sqrt{\varepsilon_1}$ change to n_1, Eq of the dielectric material (18) can be rewritten as

$$\lambda_0 = n_1\Lambda \quad (20)$$

Conclusion

- ✓ Application of voltages to the LC cell decreases the refractive index of the LC, blueshifting the transmission spectrum.
- ✓ The LC cell is an electrically controllable visible-light filter because the period of the nanoslits is 470 nm.
- ✓ If the peak transmittance and frequency tuning range of an LC cell with nanoslits are increased, the LC cell could be used to develop visible-light displays.

Acknowledgments

The authors would like to thank the Ministry of Science and Technology of Taiwan for financially supporting this research under Contract No. MOST 104-2112-M-029 -004 -MY3

Biomedical Detect by Terahertz Wave

Han-Wei Hsieh and Chia-Yi Huang*
*chiayihuang@thu.edu.tw
Department of Applied Physics, Tunghai University, Taichung, Taiwan

Abstract

Chinese herbal medicines are the supplements that we use daily to regulate the body and treat diseases. Most of the Chinese herbal medicines rely on imports, so they cannot control the quality of medicinal herbs. If environmental factors cause the heavy metal content of Chinese herbal medicines to be too high or artificially add sulfur dioxide to facilitate Save, it may cause harm to the human body. In order to allow people to eat safe Chinese medicine, we use terahertz spectrum analyzer to inspect licorice and angelica.

Theory

Terahertz radiation consists of electromagnetic waves within the band of frequencies from 0.1 to 10 terahertz(1 THz = 10^{12} Hz). Photon energy in the THz regime is less than the band-gap energy of non-metallic materials and thus THz radiation can penetrate such materials without damage. Therefore, we use THz beams transmit through Chinese medicine for our study.

Fabrication

Chinese herbal medicines are sliced by an appropriate size. Then use two pieces of PET to seal the Chinese medicine, measure the transmitted spectrum difference of the sliced samples with soaked metal ion and without metal ion. The samples are placed in a room-temperature drying oven or use a low-temperature heating to evaporate water vapor before measurement.

Results

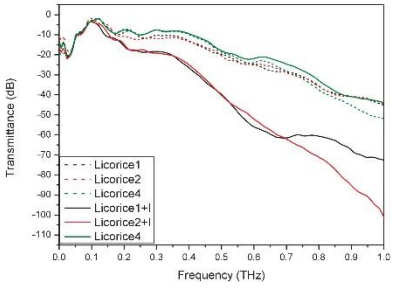

Fig. 1. Licorice is immersed in iodine 1-butyl 3-methyl ionic liquid.

As shown in Figure1, The signal of the licorice slices 1 and 2 immersed in 1-butyl-3-methyl iodinated liquid and removed moisture. detected by the Terahertz transmitted spectrum was significantly reduced.

Figure 2 shows that licorice slices were soaked in chromium nitrate and placed at room temperature for 2 hours, 4 hours, and 6 hours until the penetration signal was closer, indicating that the effect of moisture was lower and the licorice was affected by metal ions.

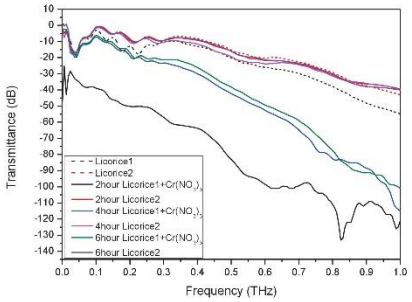

Fig. 2. Comparison of the transmitted spectrum of the licorice slices soaked with chromium nitrate for 2 hours, 4 hours, and 6 hours.

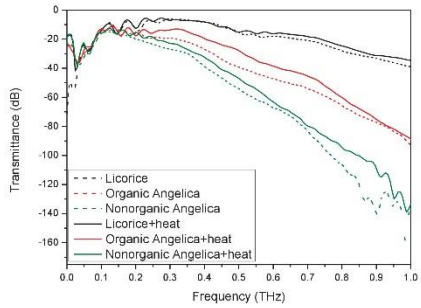

Fig. 3. Comparison of transmitted spectrum of the organic angelica, non-organic angelica and non-organic licorice after removing moisture.

Figure 3 compares the transmittance difference between organic angelica, non-organic angelica, and non-organic licorice after the three samples were heated in an oven at low temperature and the weights were measured until the moisture almost volatilized. It was found that the non-organic licorice has the lowest impact and is not susceptible to moisture when stored at room temperature.

Conclusion

Megahertz spectrum analyzers have a high frequency of radiant energy that is sensitive to metal ions, and can also test foods for anti-corrosion components.

Terahertz modulators using Ionic Liquid Cells

Hsiao-Shan Chang (張孝姍) and Chia-Yi Huang* (黃家逸)
*chiayihuang@thu.edu.tw
Department of Applied Physics, TUNGHAI UNIVERSITY, Taichung, Taiwan.

Abstract

Ionic liquids that are poured into the ITO-coated PET substrate use voltage to control the change of transmittance as a commercial terahertz spectrometer (TPS 3000, TeraView) is used to measure the transmittance of the ionic liquids. Instead of traditional metals, we use a well-conductive ionic liquid. Because of ionic liquids are easily prepared to our desired concentration. Consequently, such a cell can be used to develop intensity-switchable terahertz modulators.

Fabrication

Cut the Polyethylene terephthalate (PET) substrate into one sizes, which is 2 cm*1.5 cm. Then let PET substrates be deposited ITO. Put spacers(50um/100um) on the PET substrate and take another PET substrate covering up, and let spacers be clamped. Used AB glue to seal the cell then infuse ionic liquid. After that, we also use AB glue to seal another side of the cell, which avoid ionic liquid effluence. Stripping wire-wrapping wire silver plated clamp with self closing tweezers and then dot AB glue on the both ends of the wire and dot colloidal silver on the middle of the wire (Fig. 1). After waiting for them to get dry, setting up AC power supply and clipping wire-wrapping wire silver with alligator clip then passing voltage. Using a commercial terahertz spectrometer (TPS 3000, TeraView) to measure spectra of the cell. When we switch different voltage, we can measure different transmittance.

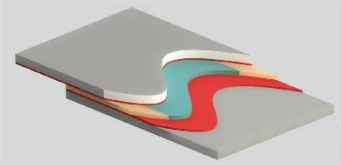

Fig. 1. Geometry of an ITO-based with ionic liquid THz modulator.

Results

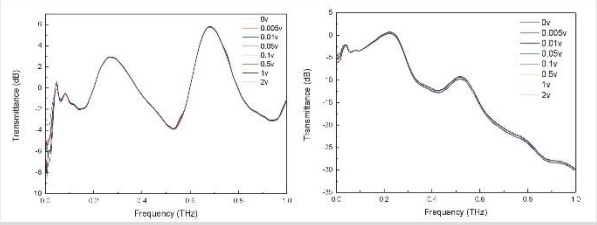

Fig. 2. Shows the relationship between transmittance and frequency and ionic liquid use 1-Butyl-3-methylimidazolium chloride. Thickness of spacers:(a)50μm (b)100μm

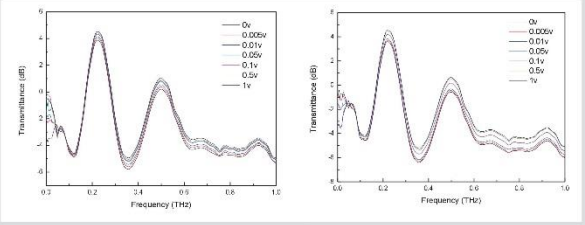

Fig. 3. Shows the relationship between transmittance and frequency and ionic liquid use $[Cu(H_2O)_4]SO_4 \cdot H_2O$. Thickness of spacers 50μm Molarity :(a)10^-9 M (b)10^-6 M

Conclusions

- This device can be used to develop terahertz modulators.
- Using $[Cu(H_2O)_4]SO_4 \cdot H_2O$ as ionic liquid is better than 1-Butyl-3-methylimidazolium chloride because it is dissociated out of 2-valent ions.

东海大學

Terahertz filters based on metamaterials deposited on plastic substrates

Jing-Ya Chiu and Chia-Yi Huang*

Dept. Applied Physics, Tunghai University, Taichung 407, Taiwan, Republic of China

Presenter: Jing-Ya Chiu

[Contact E-mail: chiayihuang@thu.edu.tw]

Abstract

This plastic substrates are widely used in different degrees of people due to their high comfort. A metamaterial layer of imprint split-ring resonator (SRR) is deposited on the surface of a polyethylene terephthalate (PET) substrate and can be imprinted by plastic substrates by imprinting technology. When the plastic substrates with SRR attached absorbs water, the film will become soft and distorted. The transmittance of the resonance gap of the metamaterial is increased with the water content. Therefore, the plastic substrates with the metamaterial can be used to develop intensity-switchable band-stop filters in the THz regime.

Theory

We use plastic substrates to imprint SRR patterns on the surface of the PET substrate. When all SRR patterns transferred to plastic substrates then we drip some reverse osmosis water (RO water) on substrates to measure signal changes.

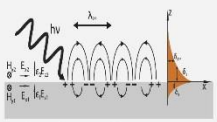

(i) surface plasmonic resonance, SPR

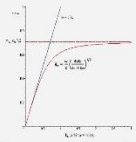

(ii) curve of dispersion

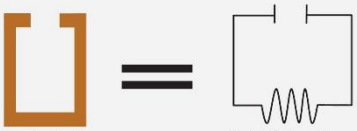

(iii) schematic of split-ring resonator (iv) *LC* circuit

Fabrication

A metallic material of silver is deposited on PET substrate by sputtering, as shown in Fig. (a). Then the photoresist (ENPI 202) layer is coated on silver and patterned as SRR structure by photo-lithography, as shown in Fig. (b). In Fig. (c), silver is wet etched by aluminum etching solution. And the patterned photoresist above patterned metallic material is removed by acetone, as shown in Fig. (d). Finally in Fig. (e) and Fig. (f), the sample is imprinted by plastic substrates to transform metal SRR patterns from PET substrate. Terahertz spectrometer (TeraView TPS3000) is used to measure the frequency domain spectrum changes of SRR on plastic substrates when it expand.

Experiment

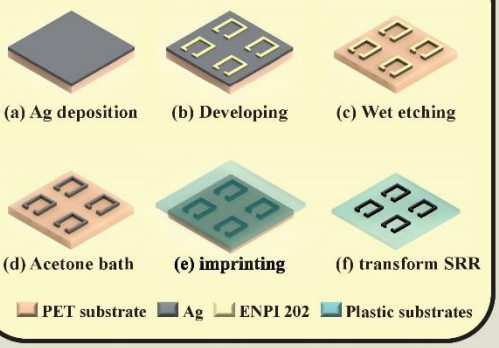

Results

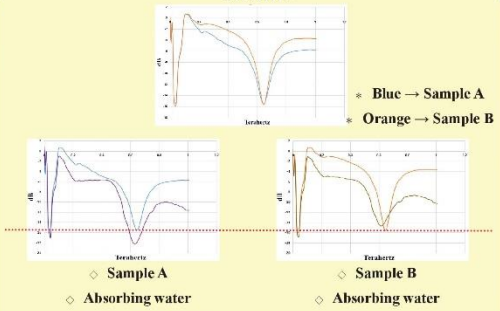

Changes of different plastic substrates samples

Conclusions

- The surfaces of plastic substrates are not completely flat when the SRR patterns are transferred to the substrate.
- Metamaterials deposited on plastic substrates can be used to measure changes in the spectra of other organic solvents.

东海大學

Passively Tunable Terahertz Metamaterials Using Nanoparticles

J. K. LIU and C. Y. Huang*

Applied Physics, Tunghai University, Taichung, Taiwan

*[Contact E-mail: chiayihuang@thu.edu.tw]

Abstract

This work uses light polymerization to fabricate nanoparticles on a glass, and then metamaterial is deposited on the glass with the nanoparticles using a metal mask. Experimental results reveal that the resonance frequency of the metamaterial with the nanoparticles is shifted from that of a metamaterial without nanoparticles because the surface area of the nanoparticles affects the electromagnetic resonance of the metamaterial. The metamaterial with the nanoparticles can be used to develop passively tunable terahertz filters.

Theory

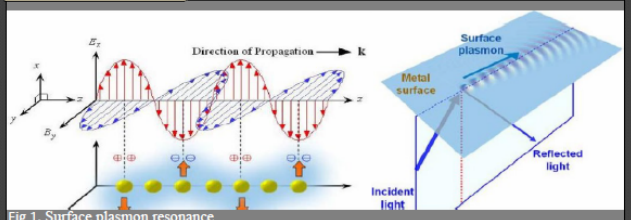

Fig 1. Surface plasmon resonance.

Mechanism

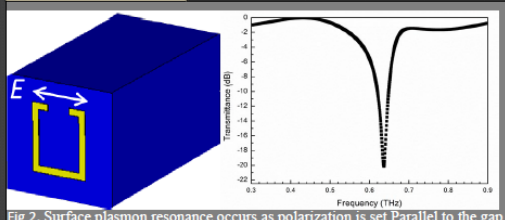

Fig 2. Surface plasmon resonance occurs as polarization is set Parallel to the gap.

Experiment

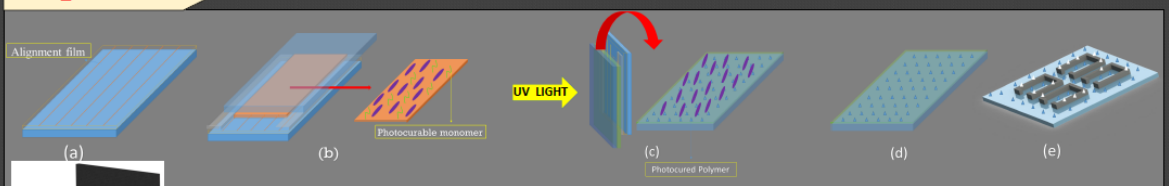

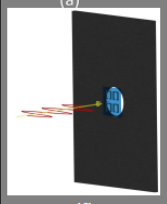

(f)

◆ Two glasses with an area of 2cm × 2cm are used in this study. After alignment films are deposited on the glasses, they are rubbed along the same direction. The glasses are sealed into an empty cell. The cell is filled with a NOA65-doped E7 mixture, and then irradiated with UV light. Nanoparticles are formed on the glasses due to light polymerization. The glasses are separated carefully. One of the glasses is deposited with a patterned silver film using a metal mask. The sample is measured using a terahertz spectrometer.

Result

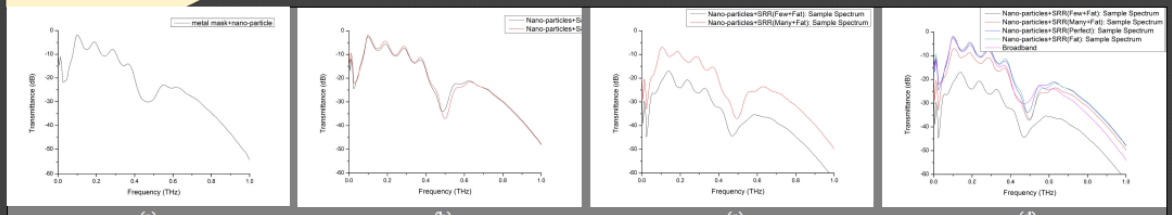

(a) (b) (c) (d)

◆ When our glass substrate (2cm × 1.5cm) measure in terahertz spectrum, we find the Broadband. Shown in (a), It's during 0.4 to 0.6 THz. The reason of the Broadband appearance is the surface of glass we modify. We ''make'' a layer of nanoparticle film that increases every SRR's length and width. Shown in (b) and (c), According to the formula (Fig 3.), it change the L, every SRR's L is different because of random size of nanoparticles. Therefore the irregular surface causes they absorb the different bands of terahertz.

Conclusion

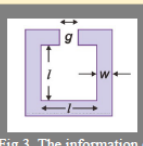

L : Inductance (A, B and W)

C : Capacitance (G and ε)

$$\omega = \frac{1}{\sqrt{LC}}$$

Fig 3. The information of SRR(Splitting resonance ring).

◆ In principle, there are many reasons of broadband appearance, we only figure out one of them. In the future, we must carry out more experiments to exclude other possible factors and ensure our conclusion. We also want to find more effective applications of this broadband.

Fishnet gratings based on photoaligned liquid crystal cells

Mi-Chia Hsu(徐彌迦), *Chia-Yi Huang**(黃家逸)

Abstract

This work fabricates a fishnet grating by exerting two one-dimensional (1D) holographic interference fields with mutually orthogonal grating vectors separately on the substrates of a dye-doped liquid crystal (DDLC) cell. The DDLC mixture in the cell includes a nematic LC, methyl red (MR) dye, and 4-methoxyazobenzene (4MAB) dye. The fishnet grating is formed because the periodical adsorption of the MR dye on the irradiated surfaces of the cell causes the anisotropic photoalignment of the LC. The fishnet grating can be erased (recovered) by the illumination of a UV (green) beam since the *trans*→*cis* (*cis*→*trans*) isomerization of the 4MAB dye causes the isothermal nematic→isotropic (isotropic→nematic) phase transition of the LC. Such a grating can be used to develop optically controllable photonic crystals. Simulated results depict that a photoresist-coated plastic substrate that is exposed to the fishnet pattern of a 2D grating can be used to develop terahertz fishnet metamaterials, and their resonance spectra can be passively tuned by moving the substrate and lens that forms the fishnet pattern during fabrication. Therefore, the mask-free photolithography can be used to fabricate passively tunable terahertz filters.

Experimental

The grating is fabricated from a DDLC cell that is exposed to a 2D interference field. The DDLC mixture in the cell is prepared using a nematic E7 LC (Merck), methyl red (MR) dye (Sigma-Aldrich), and 4-Methoxyazobenzene (4MAB) dye (Fluka). The mixing ratio of E7: MR: 4MAB in this mixture is 69:1:30 by weight. Figure 1 schematically depicts the fabrication process of a 2D LC grating.

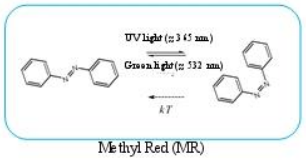

Methyl Red (MR)

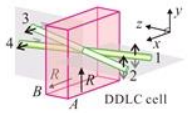

Figure 1. Fabrication of 2D LC grating

The DDLC cell, which is separated by 18μm-thick spacers, comprises glass substrate A/ DDLC mixture/ glass substrate B. The two uncoated substrates A and B are rubbed along the y and x axes of Fig. 1, respectively. The rubbed substrates exert a twisted nematic (TN) alignment of weak anchoring on the LC in the cell. Four coherent pump beams from an Ar+ laser (λ = 514.5 nm) are used to fabricate a 2D LC grating, as shown in Fig. 1. Two pump beams 1 and 2 (3 and 4) which intersect at an angle of ~1.46° in the xz (yz) plane are incident to the DDLC cell from substrate A (B), and their polarizations are along the y (x) axis. Each of the pump beams has a light intensity I_0 of 1.5 mW/cm^2. The interference formed by beams 1 and 2 (3 and 4) generates a spatial variation of light intensity on surface A (B), establishing a corresponding distribution of the adsorption of the MR dye, and causing the position-dependent surface director reorientation. The adsorbed MR dye molecules on each surface reorient the surface director toward a direction perpendicular to the interference field which acts on that surface.5,6 The director reorientations on surfaces A and B form two 1D gratings, which compose a 2D grating in the DDLC cell.

Results and discussion

A 2D grating with a spatial period of 20 μm is formed after the irradiation of 30 min. As the irradiated time is increased to 40 min, the 2D grating exhibits a fishnet pattern. Figure 2. POM images of DDLC cell that is irradiated for (a) 30 min and (b) 40 min. Upper and bottom intensity images are obtained under parallel polarizers (P//A) and crossed polarizers (P⊥A), respectively.

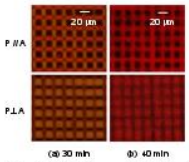

Figure 2. POM images of DDLC cell

Figure 3. Models of DDLC cell in simulation. (a) Orientations of surface directors before photoalignment. Ideal orientations of surface directors that rotate in (b) opposite directions and (c) unidirectional direction after photoalignment. $I_{1,2}$ and $I_{3,4}$ are the intensity distributions of the interferences on surfaces *A* and *B*, respectively. Λ is the spatial period of the intensity distributions.

Figure 4. Orientations of surface directors that rotate in (a) opposite directions and (b) unidirectional direction after photoalignment. The green units which neighbor the yellow unit have a lower surface free energy density under the opposite rotation than under the unidirectional rotation because the surface directors in the green units exhibit a smaller twist angle under the former than under the latter. As a result, the photoaligned cell has the relatively stable fishnet grating as the surface directors are rotated in the opposite directions.

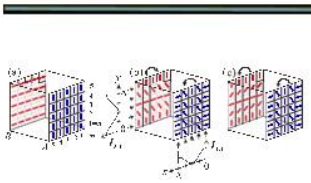

Figure 3. Models of DDLC cell in simulation

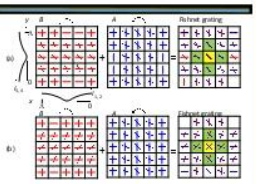

Figure 4. Orientations of surface directors that rotate

Application

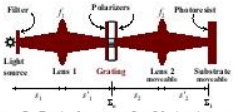

Figure 8. Optical system for fabricating passively tunable terahertz fishnet metamaterials

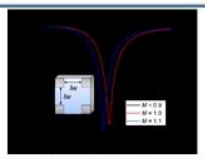

Figure 9. Simulated terahertz spectra

- **Passively tunable terahertz fishnet metamaterial:**

Fig9. Presents the simulated terahertz spectra of the reduced, normal and enlarged fishnet metamaterials at M = 0.9, 1.0 and 1.1, respectively. The resonance peaks of the reduced, normal, and enlarged fishnet metamaterials are at 11.6, 10.4 and 9.6 THz, respectively. The resonance peak of the reduced (enlarged) fishnet metamaterial is blueshifted (redshifted) from that of the normal fishnet metamaterial by 1.2 (0.8) THz.

Acknowledgements

- This research was financially supported by the Ministry of Science and Technology (MOST) of Taiwan under contract no. MOST 104-2112-M-029-004-MY3.
- Department of Applied Physics, Tunghai University, Taichung 407, Taiwan.

Controllable terahertz filters using curved liquid crystal polymer films

Wei-Yuan Chen, Chia-Yi Huang
[illegible]

Abstract

Liquid crystal polymer (LCP) films are rolled into hollow cylinders. The hollow cylinders are measured by a terahertz spectrometer. Experimental results reveal that the transmittance spectra of the hollow cylinders have peaks at specific frequencies due to the Fabry-Pérot resonance, and the frequencies of the peaks can be tuned by changing the thicknesses and rolled layers of the LCP films. Therefore, the rolled LCP films can be used to develop terahertz filters.

Fabrication

Each of empty cells comprises two glasses, which is separated by two spacers. The glasses in each empty cell are coated with rubbed polyimide layers. A LCP mixture is prepared using a nematic LC (HTW114200-100, Fusol Material), monomer (RM-257, Sigma-Aldrich) and photoinitiator (IRG-184, Sigma-Aldrich). Each empty cell is filled with the LCP mixture. After the cells are cured using a UV beam with a light intensity of 10 mW/cm^2, the LCP films are stripped from the cells. The LCP films are rolled into hollow cylinders. The hollow cylinders are measured by a terahertz spectrometer.

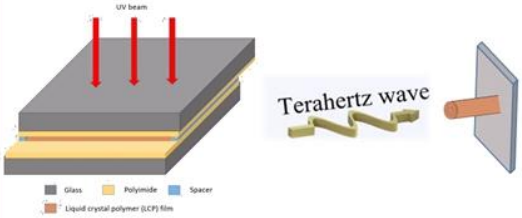

Fig. 1. Fabrication process of liquid crystal polymer films.

Results

Figure 2 presents the dependence of the terahertz spectra of the hollow cylinders with one rolled layer on the thicknesses of the LCP films. The experimental results indicate that the three hollow cylinders exhibit the peaks at different terahertz frequencies. These peaks arise from the Fabry-Pérot resonance. The hollow cylinders can be used to develop terahertz filters.

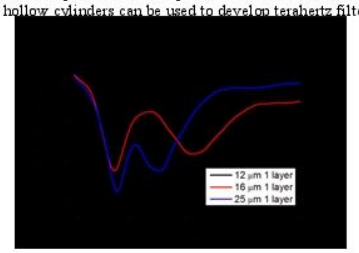

Fig 2. Dependence of terahertz spectra of hollow cylinders with one rolled layer on thicknesses of LCP films.

Figure 3 presents the dependence of the terahertz spectra of the hollow cylinders that comprise the 12mm-thick LCP films on the rolled layers. The transmittances of the main peaks decrease with the increase in the rolled layers. Therefore, the peak transmittances of the hollow cylinders can be tuned by the rolled layers.

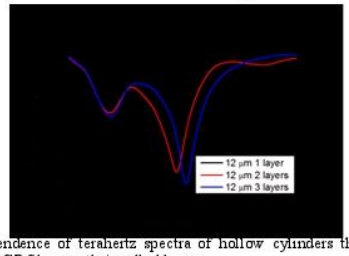

Fig. 3. Dependence of terahertz spectra of hollow cylinders that comprise 12mm-thick LCP films on their rolled layers.

Figure 4 displays the dependence of the terahertz spectra of the hollow cylinders that comprise 25mm-thick LCP films on their rolled layers. The experimental results in Fig. 4 are similar to those on Fig. 3. The experimental results in Figs. 3 and 4 depict that the transmittances of the main peaks of the hollow cylinders decrease as the thicknesses of the LCP films are increased from 12 mm to 25 mm. However, the tradeoff is that the transmittances of the spectral shoulders are also decreased.

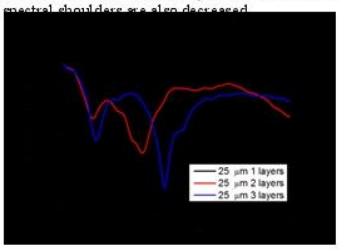

Fig. 4. Dependence of terahertz spectra of hollow cylinders that comprise 25mm-thick LCP films on their rolled layers.

Figure 5 presents the dependence of the terahertz spectra of the hollow cylinders with the three rolled layers on the thicknesses of the LCP films. Although the mail peak of the hollow cylinder that comprises the 50mm-thick LCP film has a small transmittance of -100 dB, the shoulders of the spectrum have also a low transmittance of -40 dB. Therefore, the hollow cylinder that comprises the 12mm-thick LCP film is superior to those that comprise the 25mm-thick and 50mm-thick LCP films as they are used to filter terahertz wave.

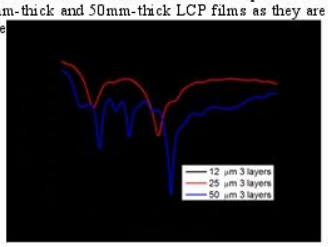

Fig 5. Dependence of terahertz spectra of hollow cylinders with three rolled layers on thicknesses of LCP films.

Conclusion

This work fabricates terahertz filters using the hollow cylinders that are rolled with the LCP films. The transmittances and frequencies of the spectral peaks of the hollow cylinders depend on the rolled layers and thicknesses of the LC films. The hollow cylinders can be used for terahertz imaging and terahertz telecommunications.

Acknowledgment

This research was financially supported by the Ministry of Science and Technology (MOST) of Taiwan under contract no. MOST 104-2112-M-029-004-MY3.

Highly sensitivity biosensors using thick metamaterials

W. Y. Chen and C. Y. Huang*
Applied Physics, Tunghai University, Taichung, Taiwan
[Contact E-mail: chiayihuang@thu.edu.tw]

Abstract

This work uses a thick metal film to fabricate a highly sensitive terahertz metamaterial. Experimental results depict that the metamaterial has a very low transmittance and small full width at half maximum at the resonance peak because the thick metal film causes the strong electromagnetic resonance. Such a metamaterial can detect the frequency shift as a thin dielectric layer is deposited on the metamaterial.

Theory

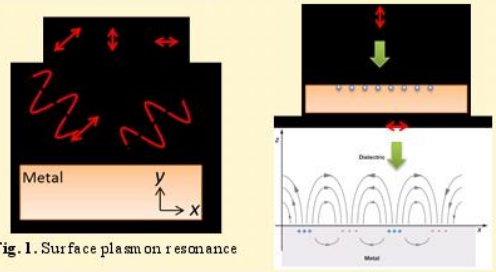

Fig. 1. Surface plasmon resonance

Simulation

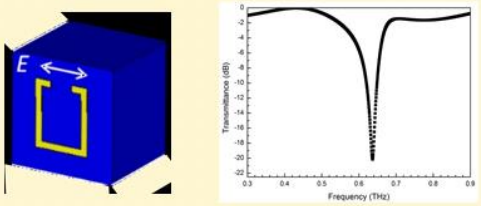

Fig. 2. These spectra are obtained using CST simulated and the polarization of normally incident terahertz waves is set parallel to the x axis.

Fabrication & Result – Liquid

Figures 3(a)-3(d) show the fabrication of SRR structures, fabricating thick metamaterials using a high-viscosity photoresist. As show in Fig. 3(e), an empty cell is fabricated by two 188μm-thick polyester (PET) substrates, which are separated by two 25μm-thick plastic spacers. Ethanol is then injected into the cells and sealed with a polymer gel to avoid liquid leakage, which is presented in Fig. 3(f).

Figure 4 shows the spectra of different samples that were measured by a terahertz spectrometer in TM mode. The samples in Figs. 4(a)-4(b) are fabricated using the same pattern in a photomask. The thin and thick metamaterials exhibit different spectral peaks since they have different metal thicknesses. The sample in Fig. 4(c) is fabricated by another pattern that can generate a resonance peak at 0.8 THz.

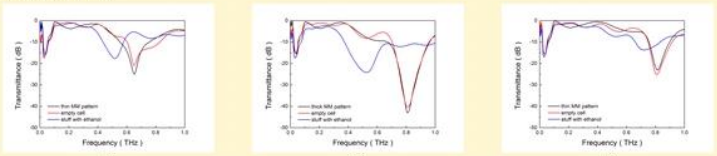

(a) (b) (c)

Fig. 4. The spectra of different samples, respectively. (a) Structure with thin metamaterials. (b) Structure with thick metamaterials. (c) Structure with thin metamaterials but different dimension.

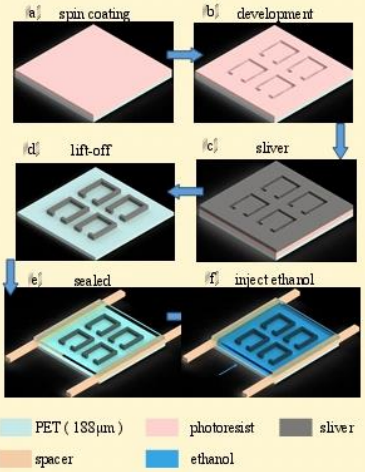

Fig. 3. The flow chart of the lithography

Fabrication & Result – BSA

Bovine serum albumin (BSA) that is dissolved in RO water is spin-coated on the SRR structures, as show in Fig. 3(d).

Figure. 5 show the spectra of different samples that were measured by a terahertz spectrometer in TM mode. Figures 5(a) and 5(b) have the same original resonance peak.

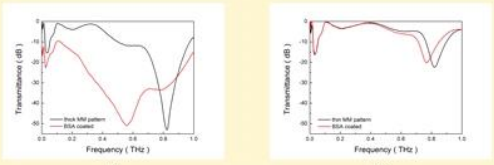

(a) (b)

Fig. 5. The spectra of different samples, respectively. (a) Structure with thick metamaterials. (b) Structure with thin metamaterials but different dimension.

Conclusions

The measured spectrum of the relatively high pattern has obviously variety of both frequency and strength. When the different dielectric materials have similar refractive index can still observed variety of strength. By these result, this kind of biosensors can have high sensitivity.

Keywords: terahertz, metamaterials, biosensors

微波對螢光奈米鑽石膜螢光的影響

指導老師:林宗欣老師　系級:光電三　專題生:李昱緯

摘要

將螢光奈米鑽石滴在微帶天線上做成螢光奈米鑽石薄膜，以微波產生器產生微波，對鑽石膜施加微波並量測螢光的強度。從光探測磁共振的實驗得知共振頻率、頻寬寬度、螢光下降比例。實驗結果得到與文獻相比較大的頻寬與較明顯的螢光強度變化。

介紹

螢光奈米鑽石中的 N-V center 受雷射連續照射下，大部分的電子處於自旋態 m=0 的能階(具有較大的電子產額)。當外加微波的頻率剛好符合基態中 m=0 與 m=±1 能階的能量差時，部分電子會跑到 m=±1 的能階，使得累積在 m=0 態的電子減少，造成螢光有明顯下降的變化，此現象稱為光探測磁共振(ODMR)。(如左邊 D 圖所示)在此工作中我們對螢光奈米鑽石薄膜施加微波，看其螢光強度對微波的反應的狀況。

實驗方法

- 以 100nm 螢光奈米鑽石作為樣品，製成螢光奈米鑽石懸浮液，並滴在微帶天線上不同的位置做成螢光奈米鑽石薄膜(圖 A)。
- 主要實驗架構是共焦式顯微鏡，連續波 532nm 雷射激發樣品並以雪崩式二極體與光子計數器收集螢光奈米鑽石訊號，同時微波訊號產生器產生微波，藉由微帶天線施加在樣品中，(圖 B)。
- 微波產生器給予 2.64GHz~2.93GHz 的工作範圍，施加頻率的微波同時測量下降後的螢光強度，觀察螢光訊號並探討微波與螢光奈米鑽石之間的關係，繪成頻率對螢光變化比例。
- 分別測量三個不同的點受微波影響的時間，從開始加微波到達平衡，甚至在到達平衡之後繼續加微波，討論微波對螢光奈米鑽石反應時間。除此之外，還做了數值模擬分析比較理論值與實驗值的差別。

圖(A)

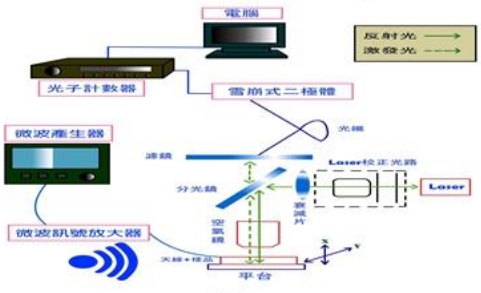

圖(B)

實驗結果

- 施加微波從 2.64GHz~2.93GHz 頻率，量測的共振頻率：2.81GHz(圖 C)，文獻記載的共振頻率：2.87GHz(圖 D)。
- 螢光強度受微波影響約有 70%的下降幅度，頻寬約 250MHz，文獻記載的微波強度受微波影響大約只有 10%，頻寬約 25MHz。

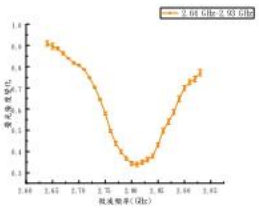

圖(C)

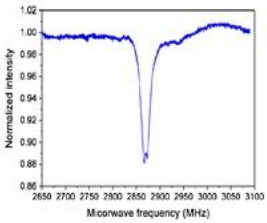

圖(D)

實驗結果與文獻記載相較之下，不管是受螢光影響下降的幅度或是頻寬皆比較明顯，我們推測螢光變化比文獻大的原因是可能是他們施加的微波強度不夠強或是施加的時間不夠久。頻寬較寬的原因，我們認為螢光奈米鑽石膜中有許多 N-V center，每個 N-V center 承受的應力並不是都相同，應力會造成氮空缺基態中 m=0、m=+1、m=-1 間能階稍微分離，造成 m=0、m=±1 間能階不同的原因，每個 N-V center 感受到的共振頻率也不一樣導致頻寬較寬。

- 在 2.81GHz 共振頻率測量反應時間，實驗值約 20 秒(圖 E)。
- 數值模擬分析螢光奈米鑽石的反應時間，理論值約 0.5 微秒(圖 F)。

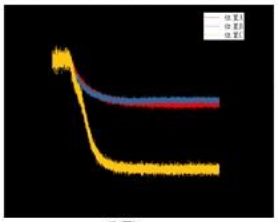

圖(E)

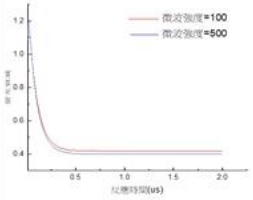

圖(F)

螢光變化的強度不同是因為接收不同微波強度造成的，雖然強度變化程度不同，但是反應時間都差不多。透過數值模擬分析，反應時間的尺度只是微秒等級，在時間的測量上與模擬出來的結果相差比較多。

結論

從光探測磁共振技術中找到共振頻率在 2.81GHz 的地方，螢光強度的變化程度將近 70%，比文獻記載的 10%明顯許多，頻率寬度比文獻寬，是因為許多氮空缺承受不同應力導致能階略有分離而造成頻寬較寬的原因。而螢光奈米鑽石反應時間約 20 秒，理論值的反應時間的尺度確只在微秒等級，可見螢光奈米鑽石薄膜對微波的反應必需要再引入其他的機制，才能有較完整的描述。

利用光散射法對高分子球作粒徑分析

指導教授:林宗欣老師 專題生:古唯佑
東海大學應用物理學系

摘要

我們利用543nm 雷射去照射樣品，當雷射光打到高分子球後，會產生散射光。我們使用High Sensitivity Light Sensor去接收散射光，並利用Vernier LabQuest 2去記錄Sensor左右的位移量和散射光強度。經由推導出來的公式回推出高分子球的粒徑大小。

原理

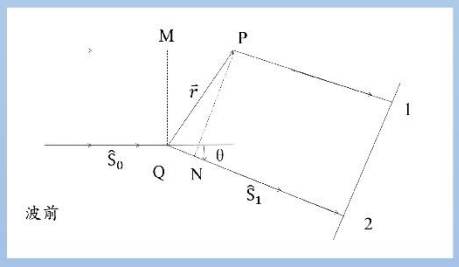

- 光打到粒子P、粒子Q後會產生散射，散射光在位置1和位置2時兩道光相位差為$\Delta\varphi = \frac{2\pi}{\lambda}\Delta X = \frac{4\pi}{\lambda}\sin\frac{\theta}{2}(\vec{r}\cdot\hat{k})$，而 $\hat{k} = \frac{(\hat{S}_0 - \hat{S}_1)}{|\hat{S}_0 - \hat{S}_1|}$
- 我們定義一個散射向量$\vec{q} = \frac{4\pi}{\lambda}\sin\frac{\theta}{2}\hat{k}$
- 兩個散射光的方程式分別為$A_1(x,t) = A_0 b_p e^{\frac{2\pi}{\lambda}i(x-vt)}$
  $A_2(x,t) = A_0 b_Q e^{\frac{2\pi}{\lambda}i(x-vt)} e^{-i\Delta\varphi}$
  其中b_1稱為散射強度。
- 假如有N個散射粒子 ，則$A_{total} - A_1 + A_2 + A_3 + \cdots\cdots + A_N$，N道光光強度總和$I \propto A \cdot A^* = \sum_{n=1}^{N}\sum_{m=1}^{N} {A_0}^2 b_n b_m e^{-i\Delta\vec{r}_{mn}\vec{q}}$
- 若為連續物質的散射$I = A_0^2 \int_{-\infty}^{\infty}\int_{-\infty}^{\infty} \rho(\vec{r}_m)\rho(\vec{r}_n) e^{-i(\vec{r}_n - \vec{r}_m)} d\tau d\tau'$
- 假設球體具有均勻散射強度密度ρ和半徑R
  $\Rightarrow I \propto \frac{9(\sin(qR) - qR\cos(qR))^2}{q^6 R^6}$
- 不同的散射角度會影響散射光光強度，利用偵測器的位置計算出散射向量$\vec{q}$，帶入上述的公式，我們便可以利用已知的光強度去計算出粒子的半徑。

實驗方法

將hybridization slide貼在載玻片上

滴入25μl稀釋1/10的高分子球溶液

蓋上蓋玻片

- 右圖為製作完成的樣品圖。下圖為光路架設圖。雷射照射樣品後，在樣品後方放上白紙當屏幕去看成像，並且利用光偵測器橫向移動去測量散射光的光強度。

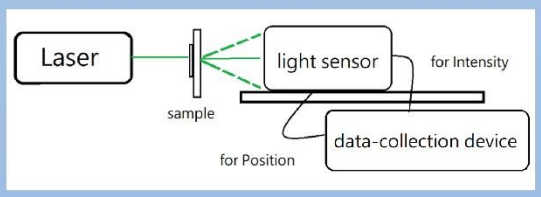

- 光偵測器可以改變不同的狹縫來量測，在光偵測器下方的滑軌能使光偵測器量測不同位置的光強度

- 數據收集設備會記錄光偵測器的位置和對應的光強度，方便之後的計算

實驗結果

- 雷射經過樣品後的散射光在屏幕上會產生一圈一圈的亮環，如圖一所示。圖二是量測散射光光強度的結果，圖中的峰值對應到了每個亮環的位置。最後我們取圖二右方的峰值去作曲線擬合，擬合出來的結果為高分子球半徑R=2.68 μm。本次擬合結果看到擬合的峰值有偏移，可能原因是光偵測器設定原點位置有誤，造成q值的計算。

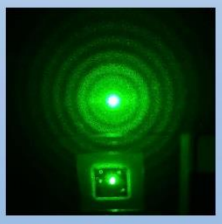

【圖一】 雷射經過樣品後的散射光在屏幕的成像

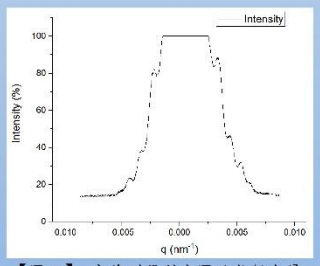

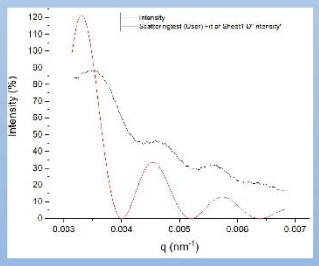

【圖二】 光偵測器對左圖的散射光量測的結果

結論

- 本次實驗結果推測高分子球的半徑為2.68 μm
- 擬合的峰值有偏移，可能是偵測器原點位置沒設定好，進而影響q值的計算

Fluorescence Stability of 4-nm Graphene Quantum Dots
4nm 石墨烯量子點螢光穩定性研究

Yung-Pin Chao (趙永斌)[1] and Tsong-Shin Lim (林宗欣)[1]
[1]*Department of Applied Physics, Tunghai University, Taichung, Taiwan*

摘要

我們對石墨烯量子點的光穩定性進行分析，發現樣品所發出的螢光強度會先下降一段後才會趨於穩定的狀態。我們也進行螢光強度下降過程中的量測，發現下降過程中的螢光光譜以及螢光生命週期皆一致，因此認為我們的樣品中只有一種發光機制，且我們認為螢光強度會下降是因為樣品邊緣的電子與氧氣反應導致光漂白的行為，實驗中也利用PVA-GQDs與GQDs作為對照驗證我們的猜測是正確的。

介紹

由於石墨烯的高品質二維晶格結構，使單層的石墨烯有著高遷移率，但由於石墨烯沒有能隙而無法發螢光，這使得其在應用上受到侷限。後來學者透過物理方法加上化學方法以及電化學的方法切割石墨烯或是石墨相關材料到量子點的大小，或是以一些綜合性的化學合成的方法製作出了石墨烯量子點(Graphene Quantum Dot, GQD)。被明顯增強的量子侷限效應以及邊界效應賦予了GQD很多優越的物理特性，使其在應用上更為廣泛。在本研究中對4nm的GQDs滴在玻片上並量測光穩定性，且在實驗中我們發現了與文獻中不同的結果，並針對不同的部分進行討論。

實驗

GQD

實驗中所用之GQD樣品其表面有一些amino、C-H、 COOH、C=O及epoxy group。為了方便量測，我們將GQD稀釋再將樣品滴在清洗過的矽基板上。

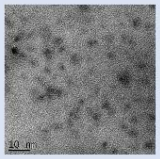

為了得知石墨烯量子點的粒徑大小，我們利用高分辨穿透式電子顯微鏡(HR-TEM)進行量測，且在較低解析度時發現樣品粒徑大小集中在4nm。

PVA-GQDs

光穩定性量測中為了要讓GQDs與氧氣隔絕，因此我們將GQDs與聚乙烯醇(Poly vinyl alcohol, PVA)水溶液混合。配置過程先將純水加熱至80 ◦C ，並將PVA粉末一邊攪拌緩慢加入，製作成重量百分濃度3%的PVA水溶液。再將PVA水溶液與GQDs水溶液以1:1的比例混合得到PVA-GQDs水溶液，最後將樣品滴在清洗過的矽基板上進行量測。

儀器架構

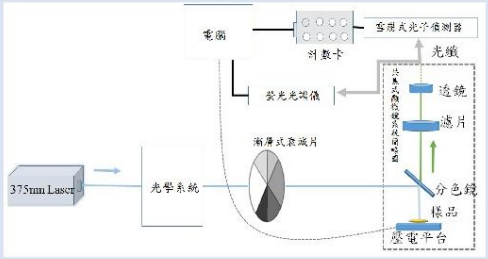

首先將波長375nm，功率約為0.185mW 的半導體紫外光連續波雷射，搭配漸層式衰減片調整雷射強度後打入共焦式顯微鏡中激發樣品，樣品被激發後發出的螢光會被顯微鏡頭收集，並通過高通濾片與透鏡，再將螢光訊號經光纖傳送到光子偵測器-雪崩式二極體量測螢光強度，或傳送到光譜儀分光量測螢光光譜儀。其中我們也將樣品放置共焦式顯微鏡的載台上，並使用共焦式顯微鏡搭配壓電平台進行局部區域的掃描。

結果

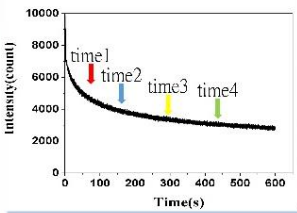

先前的文獻中提到GQDs發出的螢光強度相當穩定並不會衰減，但在我們的實驗中發現，螢光強度會先快速的下降再達趨近穩定的強度，因此我們認為螢光強度快速下降的過程中可能有不同衰減速率的發光機制，而我們亦針對強度下降的部分進行螢光光譜以及螢光生命週期的量測並分析。

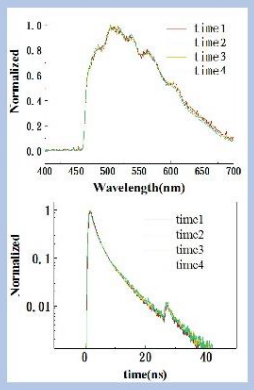

我們量測下降過程中的螢光光譜(上圖)與螢光衰減曲線(下圖)，並將兩者歸一化可清楚的看出螢光強度下降過程中的螢光光譜與螢光生命週期皆相同。這表示螢光強度下降過程中所發出的螢光皆為同一種發光機制所激發。

我們則進一步猜測造成螢光強度在一開始會有快速下降的原因為，激發的GQDs較為團聚，因此位於邊緣電子被激發時容易與空氣的氧產生反應發生光漂白的現象。

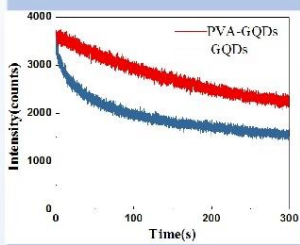

為了進一步驗證，我們將PVA水溶液與GQDs水溶液混合得到PVA-GQDs水溶液，並量測光穩定性。我們發現PVA-GQDs螢光強度比GQDs螢光強度較為穩定，是由於GQDs與PVA混合在一起後，GQDs的邊緣會被PVA覆蓋，達到與氧氣隔離的效果，而沒有與PVA泡在一起的GQDs邊緣電子在被激發時會與氧氣反應產生光漂白的行為。

結論

從先前的文獻中得知GQDs螢光強度並不會隨著時間而下降，然而在實驗中我們發現，當時間尺度較小時我們量測到GQDs被雷射激發時強度會先下降再達到一個穩定的大小，此結果與文獻中的結果不太相同。因而我們也針對螢光強度下降時進行量測，我們發現下降過程中發出的螢光以及達到穩定時所發出的螢光有相同的螢光光譜以及相同的螢光衰減曲線。我們也製作了PVA-GQDs進行光穩定性的量測與GQDs作比較，驗證了光強度之所以會快速的下降是由於邊緣的電子被激發後與氧氣反應發生光漂白所產生的現象。

獼猴複雜網路的檢測與分析

高錢生、施奇廷

東海大學應用物理系

Abstract：世上存在各種類型的網路結構，諸如交通、大腦、河流等等，將其轉換為複雜網路後，再以矩陣表示，對此矩陣進行檢測，從各種檢測中找出節點或連結在該複雜網路中的定位。在此以獼猴的腦網路為例，將其腦區轉為節點，透過檢測，可以得知其腦區被分類為4個不同的功能模組，且在這4個功能模組中，較為重要的腦區分別為AITv、V4、TE、7b。和大多複雜網路相同，此獼猴的腦網路也顯示出小世界的特性。

腦網路檢測

資料來源與特性

- 本研究所使用的獼猴大腦連結原始資料，引自獼猴大腦資料庫「CoCoMac」(R. Kötter 2004)
- 此網路將獼猴大腦分成47個區域，共有505條具有方向性、沒有權重的連結
- 連結密度為23.36%
- 分析程式採用美國印第安那大學Olaf Sporns所開發，於 MATLAB 環境下執行的「Brain Connectivity Toolbox」（BCT，Rubinov 2010）

群聚度檢測

- clustering coefficient
  在網路中計算群集的程度
  取任意節點，計算和它相連的節點是否也互相相連
  由計算三角形的數量得出

$$t_i = \frac{1}{2}\sum_{j,h\in N} A_{ij}A_{ih}A_{jh}$$

$$c_i = \frac{2t_i}{d_i(d_i-1)}$$

- Shortest path length
  任一兩相連節點 u、v 間距離為 $\frac{1}{A_{uv}}$
  另兩節點 i、j 無直接相連
  節點 i 到 j 間的Shortest pat length為

$$d_{ij} = \sum_{a_{uv}\in g_{ij}} \frac{1}{A_{uv}}$$

單一節點檢測

- Degree
  和任意一個節點 i 連線的節點個數
  可分為向內或向外的連結
  strength為degree的weighted版

in-degree	out-degree
某點指向外的連結	某點指向內的連結

- Betweenness
  任意節點 h 傳遞到節點 j 時，若中間經過節點 i，i 就加1

節點-模組關係檢測

- participation coefficient
  節點 i 和其他模組的連結程度
  $k_i(m)$ 是module中節點 i 和其他節點的連結數
  若值較低，就代表節點 i 和自己的模組連結較緊密

$$y_i = 1 - \sum_{m\in M}\left(\frac{k_i(m)}{k_i}\right)^2$$

- within-module degree z-score
  節點 i 在模組內的連結數
  和所有節點的連結平均做比較

$$z_i = \frac{k_i(m_i) - \bar{k}(m_i)}{\sigma_{k(m_i)}}$$

Results / Analysis

Modularity

- 設定C為分群，每個C對應一個Q
- 設定模組內連結較緊密
- Q是群內連結減隨機網路群內連結的期望值

[redacted]

- 結果如上表，此網路分為4個module

Small World

- 介於有序和隨機網路
- 出現在大部分網路結構中
- 同時具有高度segregated 和 integrated
- $S >> 1$ 就具有small world 結構

$$S = \frac{\gamma}{\lambda}$$

計算結果s=1.4599
雖不大，但仍具有small world 結構

- C：clustering coefficient
- L：characteristic path length
- C_{rand} and L_{rand}：隨機網路的clustering coefficient和characteristic path length

Motif

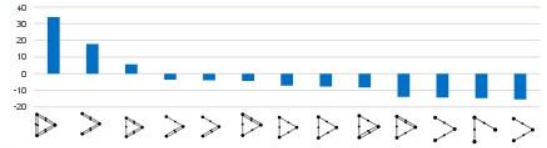

- 不同類型連結模式出現在網路中的次數
- 和隨機網路比較
- 正為比隨機網路多，負責相反

節點重要程度

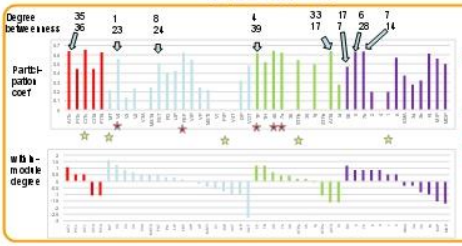

- [redacted]module[redacted]AITv、V4、TE
- 第四個module中，SII、5、7b貢獻相當
- MT、PIP、1連結不多，但betweenness高，在模組內也算相當重要

Summary and perspectives

- degree
- degree betweenness
- small world

- Motif
- participation coefficient比較，可以了解單一節點和模組的關係，從而比較出節點在網路中的重要性

References

R. Kötter, Neuroinformatics 2, 127 (2004)
M. Rubinov et al., Neuroimage 52-1059 (2010)
R. Milo et al., Science 298, 824 (2002)
D.J. Watts et al., Nature 393, 440 (1998)
M.E.J. Newman, Networks, An Introduction, Oxford University Press (2010).

東海大學應用物理系